Geometric Adaptive Control With Neural Networks for a Quadrotor in Wind Fields

Mahdis Bisheban and Taeyoung Lee, *Member, IEEE*

***Abstract*— This article presents a geometric adaptive controller for a quadrotor unmanned aerial vehicle with artificial neural networks. It is assumed that the dynamics of a quadrotor is disturbed by the arbitrary, unstructured forces and moments caused by wind. To address this, the proposed control system is augmented with the multilayer neural networks, and the weights of the neural networks are adjusted online according to an adaptive law. By using the universal approximation theorem, it is shown that the effects of the unknown disturbances can be mitigated. More specifically, under the proposed control system, the tracking errors in the position and heading directions are uniformly ultimately bounded. These are developed directly on the special Euclidean group to avoid the complexities or singularities inherent to local parameterizations. The efficacy of the proposed control system is first illustrated by numerical examples. Then, several indoor flight experiments are presented to demonstrate that the proposed controller successfully rejects the effects of wind disturbances even for aggressive, agile maneuvers.**

***Index Terms*— Adaptive control, geometric control, neural network, quadrotor unmanned aerial vehicles (UAVs), wind disturbance rejection.**

I. Introduction

MULTIROTOR unmanned aerial vehicles (UAVs) are subject to various disturbance forces and moments. In particular, wind disturbances may severely degrade the performance and stability of small aerial vehicles. Thus, it is critical to characterize these effects carefully and to alleviate them for reliable autonomous flights in various outdoor environments. Several approaches have been considered to address this problem, such as comprehensive aerodynamic modeling of wind effects, system identification of wind effect modeling parameters, and feedback control systems to mitigate the wind effects.

Concerning the wind effect modeling, thrust and drag forces in forward flights for a quadrotor UAV are studied in [1], and it is shown that the assumptions for hovering the flight models become deteriorated when the relative wind speed is sufficiently large. In [2], the blade-flapping response of a small-stiff propeller under wind is studied with a rotor–pendulum system. Once a mathematical model for wind effects is determined, the modeling parameters should be identified by experiments with the particular UAV under consideration. To determine the unknown aerodynamic modeling parameters, [3] and [4] present computational geometric approaches for the system identification of the quadrotor dynamics, where the system-identification problem is converted into an optimization problem to minimize the discrepancy between the identified model and the actual response.

To reject the undesired effects of wind disturbances, control systems are proposed to cancel out the wind effects from the mathematical models. In [5], a lookup table is used to estimate the wind forces and moments in real time based on the relative wind speed and rotational speed of the propellers. The table is generated by solving intensive computational aerodynamic expressions. Bangura and Mahony [6] present the dynamics of a brushless DC motor that is constructed to determine the power level to follow a given desired trajectory while rejecting the axial wind effects. In [7], the wind velocity data from the flow probes are used in a control system to guarantee stability in the presence of wind. While these cancellation techniques have been successful, the robustness and performance are limited by the accuracy of the wind effect model used in the controller and the estimated wind velocity. The control force and moment that resist wind would be reliable within the flight envelop considered for the aerodynamic modeling, which is additionally limited by the computing resources available in real time. Furthermore, they may deteriorate for the unexpected wind gusts, as there is no mechanism to adjust the modeling errors online.

On the other hand, several alternative control techniques have been presented without relying on cancellation. For example, [8] presents a geometric proportional–integral–derivative controller on the special Euclidean group to reject the unknown, fixed uncertainties. In addition, parametric uncertainties are addressed with a geometric adaptive control scheme in [9]. In [10], to overcome the effects of modeling errors, the data of the successive indoor experimental trials are used to tune the control parameters for aggressive maneuvers. Nicol *et al.* [11] presents an adaptive neural network for the reduced dynamics of a quadrotor UAV.

This article proposes a geometric adaptive control scheme for a quadrotor UAV, where the effects of wind are considered as unstructured, unknown disturbances. Instead of counterbalancing those with an aerodynamic model and a

Manuscript received March 18, 2019; revised October 24, 2019 and April 6, 2020; accepted June 5, 2020. Manuscript received in final form June 28, 2020. This work was supported in part by the NSF under Grant CNS-1837382 and in part by the Air Force Office of Scientific Research (AFOSR) under Grant FA9550-18-1-0288. Recommended by Associate Editor A. Serrani. *(Corresponding author: Mahdis Bisheban.)*

The authors are with the Mechanical and Aerospace Engineering Department, George Washington University, Washington, DC 20052 USA (e-mail: mbshbn@gwu.edu; tylee@gwu.edu).

Color versions of one or more of the figures in this article are available online at http://ieeexplore.ieee.org.

Digital Object Identifier 10.1109/TCST.2020.3006184

measured wind velocity, wind disturbances are compensated by an artificial neural network whose weight parameters are adjusted in real time. More specifically, we adopt the geometric controller proposed in [12] and augment it with multilayer neural networks and an adaptive law to mitigate the unknown disturbing forces and moments that are considered as an arbitrary function of the quadrotor UAV's states. The dynamics of a quadrotor is globally formulated on the special Euclidean group to avoid the singularities and complexities inherent to the Euler angles or quaternions. It is shown that the tracking errors are uniformly, ultimately bounded with an ultimate bound that can be reduced arbitrarily up to any desired precision. These are illustrated by numerical examples with the simulated aerodynamic effects of wind. Next, we show that the proposed geometric adaptive controller can mitigate wind effects even for aggressive maneuvers through indoor flight experiments with artificial wind gusts generated by an industrial fan. The preliminary results are presented in [13]. However, this article presents a complete Lyapunov stability proof, extensive numerical examples, and additional flight experimental results.

In short, the main contribution of this article is presenting a geometric adaptive controller based on neural networks for a quadrotor that is capable of compensating the unknown aerodynamic forces and moments caused by wind. This requires neither the precise mathematical model of wind effects nor the actual wind velocity, and it can be implemented without an additional onboard anemometer.

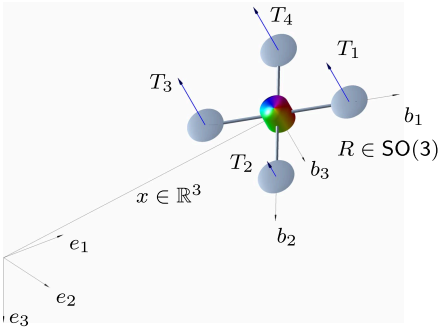

Fig. 1. Quadrotor model with the illustration of the rotors' thrust (T_1, T_2, T_3, and T_4), the inertial frame (e_1, e_2, and e_3), and the body-fixed frame (b_1, b_2, and b_3). The third inertial axis e_3 points downward along the gravity, and the third body-fixed axis b_3 is opposite to the direction of thrust [12].

TABLE I
SUMMARY OF NOTATIONS

Notation	Refers to
$\hat{}$	hat map
$\vee$	vee map
$\bar{}$	estimated value
$\tilde{}$	estimation error value
$\dot{}$	time derivative
$'$	alternative value
$\times$	cross product
$\|\|\|$	Frobenius norm of a matrix, and 2-norm of a vector
$\lambda_m()$	minimum eigenvalue of a matrix
$\lambda_M()$	maximum eigenvalue of a matrix

II. Problem Formulation

A. Quadrotor Dynamics With Disturbances

This section formulates the quadrotor dynamics, including unknown disturbances in the translational dynamics and rotational dynamics. The disturbances are considered as arbitrary forces and moments, and they may represent the wind disturbance effects, which are discussed later in Section IV. The quadrotor UAV is regarded as a rigid body with a configuration that is represented by the center of mass $x \in \mathbb{R}^3$ in the inertial frame and the orientation of the body-fixed frame with respect to the inertial frame $R \in \mathsf{SO(3)} = \{R \in \mathbb{R}^{3\times3} \,|\, R^{\mathrm{T}}R = I_{3\times3}, \det[R] = +1\}$, as illustrated in Fig. 1. Both the frames are right-handed coordinate frames. Thus, the configuration space of a quadrotor is the special Euclidean group $\mathsf{SE(3)}$, which is the semidirect product of $\mathsf{SO(3)}$ and $\mathbb{R}^3$.

The equations of motion are given by

$$\dot{x} = v \tag{1}$$
$$m\dot{v} = U_e \tag{2}$$
$$\dot{R} = R\hat{\Omega} \tag{3}$$
$$J\dot{\Omega} + \Omega \times J\Omega = M_e \tag{4}$$

where $U_e \in \mathbb{R}^3$ is the resultant force resolved in the inertial frame and $M_e \in \mathbb{R}^3$ is the resultant moment resolved in the body-fixed frame. The mass and the inertia matrix are denoted by $m \in \mathbb{R}$ and $J \in \mathbb{R}^3$, respectively. The vector $v \in \mathbb{R}^3$ is the linear velocity in the inertial frame, and $\Omega \in \mathbb{R}^3$ is the angular velocity resolved in the body-fixed frame. The hat map $\wedge : \mathbb{R}^3 \to \mathfrak{so}(3)$ is defined such that $\hat{x}y = x \times y$ and $(\hat{x})^{\mathrm{T}} = -\hat{x}$ for any $x, y \in \mathbb{R}^3$. The inverse of the hat map is denoted by the vee map $\vee : \mathfrak{so}(3) \to \mathbb{R}^3$.

Suppose that $d_h \in \mathbb{R}^+, d_v \in \mathbb{R}$ specify the horizontal and vertical distances from the origin of the body-fixed frame to the center of a rotor. If a rotor is above the origin, d_v is positive, and it is negative otherwise. The locations of the four rotors in the body-fixed frame are given by

$$r_1 = \left[d_h, 0, d_v\right]^{\mathrm{T}}, \quad r_2 = \left[0, d_h, d_v\right]^{\mathrm{T}} \tag{5}$$
$$r_3 = \left[-d_h, 0, d_v\right]^{\mathrm{T}}, \quad r_4 = \left[0, -d_h, d_v\right]^{\mathrm{T}}. \tag{6}$$

Let the thrust $T'_j \in \mathbb{R}$ and torque $Q'_j \in \mathbb{R}$ of the jth motor be given by

$$T'_j = C'_T\omega_j^2, \quad Q'_j = C'_Q\omega_j^2 \equiv C_{TQ}T'_j \tag{7}$$

where $C'_T, C'_Q \in \mathbb{R}$ are the constant thrust and torque coefficients, and $C_{TQ} = (C'_Q/C'_T) \in \mathbb{R}$ determines the relation between the reactive torques and thrusts. The resultant force and moment acting on a quadrotor can be written as

$$U'_e = mge_3 - fRe_3 - \Delta_1 \tag{8}$$
$$M'_e = \Sigma_{j=1}^4 r_j \times T'_j e_3 - (-1)^{j+1}Q'_j e_3 - \Delta_2 \tag{9}$$

where $f = \Sigma_{j=1}^4 T_j \in \mathbb{R}$ is the sum of the four rotor thrusts and mge_3 is the gravitational force with $e_3 = [0, 0, 1] \in \mathbb{R}^3$. The sums of the unknown disturbing forces and moments are denoted by Δ_1 and $\Delta_2 \in \mathbb{R}^3$, respectively.

B. Position Tracking Control Problem

Suppose that the desired position trajectory is given as a smooth function of time, i.e., $x_d(t) \in \mathbb{R}^3$. It is considered that $x_d(t)$ and all its time derivatives are bounded. In addition, it is sufficiently distinct from the gravitational acceleration such that

$$\|\ddot{x}_d - ge_3\| > B_g \tag{10}$$

for a positive constant B_g. We wish to design a control system for the rotor thrusts such that the actual position trajectory asymptotically follows the desired values in the presence of unknown disturbances. Instead of designing the rotor thrusts, the control input is considered as the total thrust f, and moment $M = [M_1, M_2, M_3]^{\mathrm{T}} \in \mathbb{R}^3$ in the body-fixed frame. For a given (f, M), the equivalent thrust of each rotor can be computed by

$$\begin{bmatrix} T_1' \\ T_2' \\ T_3' \\ T_4' \end{bmatrix} = \frac{1}{4} \begin{bmatrix} 1 & 0 & \frac{2}{d_h} & -\frac{1}{C_{TQ}} \\ 1 & -\frac{2}{d_h} & 0 & \frac{1}{C_{TQ}} \\ 1 & 0 & -\frac{2}{d_h} & -\frac{1}{C_{TQ}} \\ 1 & \frac{2}{d_h} & 0 & \frac{1}{C_{TQ}} \end{bmatrix} \begin{bmatrix} f \\ M_1 \\ M_2 \\ M_3 \end{bmatrix}. \tag{11}$$

III. Geometric Adaptive Controller With Neural Networks

In this section, we present a geometric adaptive control system for a quadrotor to reject the effects of unknown disturbances without any prior knowledge.

A. Controller Structure

The presented quadrotor dynamics is underactuated, as there are four control inputs. In [12], a geometric control system for a quadrotor is presented with a backstepping approach, which is adopted in this article. The overall controller structure is summarized as follows. Let the tracking errors in the position and the velocity be

$$e_x = x - x_d, \quad e_v = v - \dot{x}_d. \tag{12}$$

For the positive controller gains k_x, k_v, consider an ideal control force $A \in \mathbb{R}^3$ defined as

$$A = \bar{\Delta}_1 - k_x e_x - k_v e_v - mge_3 + m\ddot{x}_d \tag{13}$$

where $\bar{\Delta}_1 \in \mathbb{R}^3$ is an adaptive control term to mitigate the effects of the disturbance Δ_1. The control objective can be achieved by replacing the control force term $-fRe_3$ in (8) with the above ideal value of A. However, that is not feasible, as the total control thrust is always in the opposite direction of the third body-fixed axis, i.e., the direction of the total thrust is always $-Re_3$, and only its magnitude f can be adjusted arbitrarily.

To address this, an attitude controller is introduced such that the actual attitude is guided toward the ideal thrust direction

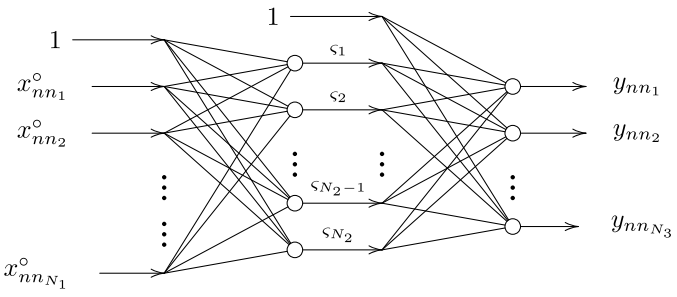

Fig. 2. Structures of a three-layer neural network.

defined by (13). More specifically, the desired direction for the third body-fixed axis is given by

$$b_{3c} = -\frac{A}{||A||}. \tag{14}$$

As it is a 2-D unit vector, the desired heading direction, namely, $b_{1_d}(t) \in \mathsf{S}^2 = \{q \in \mathbb{R}^3 \,|\, \|q\| = 1\}$, is further introduced as a function of time. These yield the complete desired attitude as

$$R_c = \left[b_{1_c}, b_{2_c}, b_{3_c}\right] \tag{15}$$

where $b_{1_c} = b_{2_c} \times b_{3_c}$, $b_{2_c} = -(b_{1_d} \times b_{3_c})/(\|b_{1_d} \times b_{3_c}\|)$. One can show that the above construction guarantees $R_c \in \mathsf{SO(3)}$, and by taking its time derivative, the desired angular velocity can be constructed as

$$\Omega_c = \left(R_c^{\mathrm{T}} \dot{R}_c\right)^{\vee}. \tag{16}$$

Any attitude tracking control system can be implemented to follow asymptotically R_c, and the total thrust is chosen as the ideal control force projected to the instantaneous thrust direction as follows:

$$f = -A^{\mathrm{T}} R e_3 \tag{17}$$

$$M_c = \bar{\Delta}_2 - k_R e_R - k_\Omega e_\Omega + \Omega \times J\Omega - J\left(\hat{\Omega} R^{\mathrm{T}} R_c \Omega_c - R^{\mathrm{T}} R_c \dot{\Omega}_c\right) \tag{18}$$

where k_R, k_Ω are the positive attitude control gains, and the tracking errors for the attitude and the angular velocity are given by

$$e_R = \frac{1}{2}\left(R_c^{\mathrm{T}} R - R^{\mathrm{T}} R_c\right)^{\vee}, \quad e_\Omega = \Omega - R^{\mathrm{T}} R_c \Omega_c. \tag{19}$$

In addition, $\bar{\Delta}_2 \in \mathbb{R}^3$ denotes an adaptive term to eliminate the effects of the unknown disturbance Δ_2 in (9). The above attitude tracking error can be interpreted as the gradient of the following attitude error function:

$$\Psi(R, R_c) = \frac{1}{2}\mathrm{tr}\left[I_{3\times 3} - R_c^{\mathrm{T}} R\right] \tag{20}$$

which is positive-definite about $R = R_c$ [12]. In addition, the angular velocity error vector satisfies $\dot{\Psi} = e_R^{\mathrm{T}} e_\Omega$.

In the absence of the disturbances and the adaptive control terms, local exponential stability has been established in [12]. Next, we will formulate the expression for the adaptive terms and the adaptive control law to address the unknown disturbances.

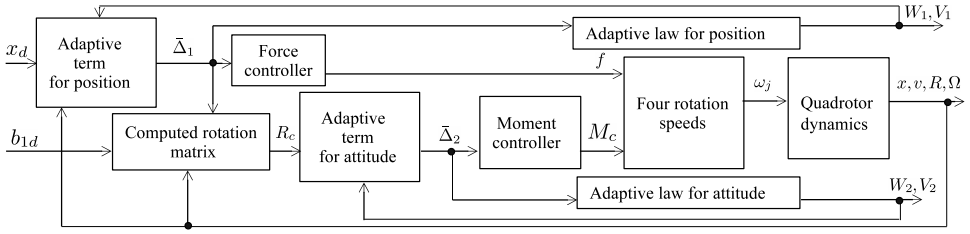

Fig. 3. Adaptive controller structure [the adaptive term for the position and the attitude dynamics is given by (23); the force controller is given by (17); the computed rotation matrix is given by (15); the moment controller is given by (18); the adaptive law is given by (24)–(27); four commanded rotation speeds are given by (7) and (11); and the quadrotor dynamics are given by (1)–(4)].

B. Adaptive Neural Network Structure

Consider a three-layer artificial neural network, as illustrated in Fig. 2. The numbers of neurons at the input, hidden, and output layers are denoted by $N_1 + 1$, $N_2 + 1$, and N_3, respectively. The input to the neural network is arranged in a vector form $x_{nn} \in \mathbb{R}^{N_1+1}$ as $x_{nn} = [1, x_{nn_1}^{\circ}, \ldots, x_{nn_{N_1}}^{\circ}]$. The input to the hidden layer, namely, $z \in \mathbb{R}^{N_2}$, is a weighted sum of the above, given by $z = V^{\mathrm{T}} x_{nn}$, for a weighting matrix $V \in \mathbb{R}^{N_1+1 \times N_2}$. The output $y \in \mathbb{R}^{N_3}$ of the neural network is $y = W^{\mathrm{T}}\sigma(z)$, where the weighting matrix of the output layer is denoted by $W \in \mathbb{R}^{N_2+1 \times N_3}$, and the activation function $\sigma : \mathbb{R}^{N_2} \to \mathbb{R}^{N_2+1}$ is defined as $\sigma(z) = [1, \varsigma_1, \ldots, \varsigma_{N_2}]$ for the sigmoid function $\varsigma_k = 1/(1 + e^{-z_k})$, for $k \in \{1, \ldots, N_2\}$.

We assume that the unknown disturbing force and moment, namely, (Δ_1, Δ_2) in (8) and (9), are dependent on the quadrotor states. According to the universal approximation theorem [14], there exist artificial neural networks that approximate these disturbances up to an arbitrary level of accuracy.

More explicitly, the particular structures of the artificial neural networks used in this article are defined as follows. Throughout the remainder of this article, the subscript $i = 1$ denotes the position dynamics and $i = 2$ denotes the attitude dynamics. Let the input to the neural network $x_{nn_i} \in \mathbb{R}^{N_{1_i}+1}$ be

$$x_{nn_i} = \left[1, x_{1_i}, x_{2_i}\right] \tag{21}$$

where $x_{1_1} = x$, $x_{2_1} = v$ are for the position dynamics and $x_{1_2} = E(R)^{\mathrm{T}}$, $x_{2_2} = \Omega$ are for the attitude dynamics. The vector $E(R) = [\theta, \phi, \psi]$ contains the Euler angles from the rotation matrix R. Consequently, $N_{1_1} = N_{1_2} = 6$. Since the neural network is formulated to approximate the disturbing force and moment, the number of outputs is $N_{3_1} = N_{3_2} = 3$. The universal approximation theorem implies that there exists an ideal value of the weighting parameters (W_i, V_i) and the number of the hidden layer N_2 such that $\Delta_i = W_i^{\mathrm{T}}\sigma(V_i^{\mathrm{T}} x_{nn_i}) + \epsilon(x_{nn_i})$, for the approximation error satisfying $\|\epsilon(x_{nn_i})\| \le \epsilon_N$ for some $\epsilon_N > 0$.

While the ideal values (W_i, V_i) are not available, it is assumed that the upper bounds $W_{M_i}, V_{M_i} > 0$ are given such that

$$||W_i|| \le W_{M_i}, \quad ||V_i|| \le V_{M_i}. \tag{22}$$

Let $(\bar{W}_i, \bar{V}_i)$ be the current estimate of the ideal weighting matrices. The adaptive control terms in (13) and (18) are computed by

$$\bar{\Delta}_i = \bar{W}_i^{\mathrm{T}}\sigma(\bar{z}_i) \tag{23}$$

with $\bar{z}_i = \bar{V}_i^{\mathrm{T}} x_{nn_i}$. In addition, they are updated according to the following adaptive law:

$$\dot{\bar{W}}_i = \begin{cases} \dot{\bar{W}}_i', & \text{if } \left\|\bar{W}_i\right\| < W_{M_i} \text{ or} \\ & \left(\left\|\bar{W}_i\right\| = W_{M_i},\ \dot{\bar{W}}_i^{\mathrm{T}}\bar{W}_i \le 0\right) \\ \left[I_W - \dfrac{\bar{W}_i \bar{W}_i^{\mathrm{T}}}{\bar{W}_i^{\mathrm{T}}\bar{W}_i}\right]\dot{\bar{W}}_i', & \text{otherwise} \end{cases} \tag{24}$$

$$\dot{\bar{V}}_i = \begin{cases} \dot{\bar{V}}_i', & \text{if } \left\|\bar{V}_i\right\| < V_{M_i} \text{ or} \\ & \left(\left\|\bar{V}_i\right\| = V_{M_i},\ \dot{\bar{V}}_i^{\mathrm{T}}\bar{V}_i \le 0\right) \\ \left[I_V - \dfrac{\bar{V}_i \bar{V}_i^{\mathrm{T}}}{\bar{V}_i^{\mathrm{T}}\bar{V}_i}\right]\dot{\bar{V}}_i', & \text{otherwise} \end{cases} \tag{25}$$

where $I_W \in \mathbb{R}^{N_{2_i}+1 \times N_{2_i}+1}$ and $I_V \in \mathbb{R}^{N_{1_i}+1 \times N_{1_i}+1}$ are the identity matrices. These correspond to the following adaptive laws projected to a bounded region satisfying (22) [15]:

$$\dot{\bar{W}}_i' = -\gamma_{w_i}\left[\sigma(z_i)a_i^{\mathrm{T}} - \sigma'(z_i)z_i a_i^{\mathrm{T}}\right] - \kappa_i \gamma_{w_i}\bar{W}_i \tag{26}$$

$$\dot{\bar{V}}_i' = -\gamma_{v_i} x_{nn_i}\left[\sigma'(z_i)^{\mathrm{T}}\bar{W}_i a_i\right]^{\mathrm{T}} - \kappa_i \gamma_{v_i}\bar{V}_i \tag{27}$$

$$a_1 = e_v + c_1 e_x, \quad a_2 = e_\Omega + c_2 e_R \tag{28}$$

for the positive adaptive gains and parameters $\gamma_{w_i}, \gamma_{v_i}, \kappa_i, c_1, c_2 \in \mathbb{R}^+$.

The proposed design of the adaptive law is based on the following expressions of the estimation errors. Let the errors in the weighting parameters be denoted by

$$\tilde{W}_i = W_i - \bar{W}_i, \quad \tilde{V}_i = V_i - \bar{V}_i. \tag{29}$$

The output error of the neural network $\tilde{\Delta}_i = \Delta_i - \bar{\Delta}_i$ can be written as

$$\tilde{\Delta}_i = \tilde{W}_i^{\mathrm{T}}\left[\sigma(\bar{z}_i) - \sigma'(\bar{z}_i)\bar{z}_i\right] + \bar{W}_i^{\mathrm{T}}\sigma'(\bar{z}_i)\tilde{z}_i - w_i \tag{30}$$

$$w_i = -\tilde{W}_i\sigma'(\bar{z}_i)z_i - W_i^{\mathrm{T}}\mathcal{O}(\tilde{z}_i) - \varepsilon\left(x_{nn_i}\right) \tag{31}$$

$$\mathcal{O}(\tilde{z}_i) = \sigma(z_i) - \sigma(\bar{z}_i) - \sigma'(\bar{z}_i)\tilde{z}_i \tag{32}$$

where $\tilde{z}_i = \tilde{V}_i^{\mathrm{T}} x_{nn_i}$. Furthermore, it can be shown that w_i is bounded by

$$\|w_i\| \le C_{1_i} + \left\|\tilde{Z}_i\right\|\left(C_{2_i} + C_{3_i}\left\|x_{1_i}\right\| + C_{4_i}\left\|x_{2_i}\right\|\right) \tag{33}$$

where $C_{k_i}, k \in 1, \ldots, 4$ are the positive constants and $\tilde{Z}_i = \mathrm{diag}[\tilde{W}_i, \tilde{V}_i] \in \mathbb{R}^{N_{2_i}+N_{1_i}+2, N_{2_i}+N_{3_i}}$ [16].

The resulting stability properties of the proposed control system, shown in Fig. 3, are summarized as follows.

Proposition 1: Consider the control force f and moment M_c defined at (17), (18). Suppose that the initial condition satisfies

$$\Psi(R(0), R_d(0)) \leq \psi_1 < 1 \tag{34}$$

for the fixed constants ψ_1, there exist the values of the controller parameters such that all the tracking errors of the quadrotor, as well as the neural network weight errors, are uniformly ultimately bounded.

Proof: See the Appendix. ∎

This theorem implies that arbitrary disturbing forces and moments can be mitigated by the adaptive neural networks that are adjusted online to cancel out the disturbances. The resulting controller does not achieve stability in the sense of Lyapunov or attractivity, as the universal approximation theorem implies approximation up to a small bounded error. Compared with the conventional adaptive control, it is not required that the uncertain term follows the form of linear regression. As such, the proposed adaptive control scheme can deal with a large class of unstructured uncertainties. In contrast to nonlinear robust controls, such as that presented in [17], there is no chattering problem in the control inputs.

IV. Numerical Example

The efficacy of the proposed control system is illustrated by numerical examples. In particular, we consider a scenario where the quadrotor is flying under wind gusts. To simulate the effects of wind disturbances, we first present an aerodynamic model of a quadrotor, inspired by the literature in the helicopter rotor dynamics.

A. Quadrotor Dynamics Under Wind Disturbance

Suppose that the wind vector presented in the inertial frame is denoted by $v_w \in \mathbb{R}^3$. The relative wind on the jth rotor in the body-fixed frame is denoted by $v_{w_j} = [u_{1_j}, u_{2_j}, u_{3_j}]^{\mathrm{T}}$. It is caused by the wind vector and the quadrotor translational and rotational velocities as follows:

$$v_{w_j} = R^{\mathrm{T}}(v_w - v) + \hat{\Omega} r_j. \tag{35}$$

The resultant external force acting on the quadrotor is given by

$$U_e = mge_3 - C_d||v - v_w||(v - v_w) + R\Sigma_{j=1}^4 T_j d_j \tag{36}$$

where the second term on the right-hand side represents the drag force acting on the center of mass and $C_d \in \mathbb{R}$ is the drag coefficient.

The variable T_j represents the thrust for the jth rotor, given by

$$T_j = C_{T_j} \rho A_p \left(r_p \omega_j\right)^2 \tag{37}$$

where $\rho \in \mathbb{R}$ is the air density and the rotor's sweeping area is given by $A_p = (\pi r_p)^2$ for the radius r_p. The rotating speed is shown by ω_j. The parameter $C_{T_j} \in \mathbb{R}$ represents the thrust coefficient and it follows the following expressions that model the effects of the induced velocity [18]:

$$C_{T_j} = \frac{sC_{l\alpha}}{2}\left[\theta_0\left(\frac{1}{3} + \frac{\mu_{x_j}^2}{2}\right) - \frac{1}{2}\left(\lambda_j + \mu_{z_j}\right)\right] \tag{38}$$

$$\lambda_j = \frac{C_{T_j}}{2\sqrt{\mu_{x_j}^2 + \left(\lambda_j + \mu_{z_j}\right)^2}} \tag{39}$$

$$\mu_{x_j} = \frac{\sqrt{u_{1_j}^2 + u_{2_j}^2}}{\omega_j r_p}, \quad \mu_{z_j} = \frac{u_{3_j}}{\omega_j r_p} \tag{40}$$

where $\lambda_j \in \mathbb{R}$ is the inflow ratio, which is the induced air velocity over the rotor tip speed, and $s = (N_b c)/(\pi r_p) \in \mathbb{R}$ is the solidity ratio, which is the approximated blade area over the blade's sweeping area. Next, c, N_b represent the blade chord and the number of blades for one rotor, respectively. The blade lift curve slope and the blade pitch angle are shown by $C_{l\alpha}, \theta_0 \in \mathbb{R}$. In addition, μ_{z_j}, μ_{x_j} are the perpendicular and parallel advance ratios to the rotor plane. As described above, C_{T_j} is defined implicitly. Therefore, Newton's iterative method is used in the numerical simulation to obtain the thrust coefficient and the inflow ratio.

Next, we consider the blade-flapping effects corresponding to the thrust direction's change due to the wind velocity parallel to the rotor plane. In (36), the rotor thrust's direction in the body-fixed frame is denoted by the unit vector $d_j \in \mathbb{S}^2$, and it is computed by

$$d_j = \left[\frac{-\sin\alpha_j}{\sqrt{u_{1_j}^2 + u_{2_j}^2}} u_{1_j}, \frac{-\sin\alpha_j}{\sqrt{u_{1_j}^2 + u_{2_j}^2}} u_{2_j}, -\cos\alpha_j\right]^{\mathrm{T}} \tag{41}$$

where the blade-flapping angle of the jth rotor is shown by $\alpha_j \in \mathbb{R}$. If the first and second elements of the relative wind vector become zero, i.e., $u_{1_j}, u_{2_j} = 0$, then $d_j = -e_3$, implying that there is no thrust component in the b_1–b_2 plane. Let $C_\alpha \in \mathbb{R}$ be the fixed flapping-angle coefficient [19], [20]. Then, the flapping angle can be approximated with

$$\alpha_j = C_\alpha \sqrt{u_{1_j}^2 + u_{2_j}^2}. \tag{42}$$

If the vertical distances from the origin of the body-fixed frame to the center of a rotor, d_v, are not zero, then the deflected force results in moments in the b_1 and b_2 directions. Hence, (11), which is used in the controller developments, becomes invalid. Because of the difficulties in measuring the flapping-angle coefficient, it is not practical to compensate for the force and moments directly due to the flapping angles in the controller. As such, each rotor's thrust command is still computed by (11) in the implementation of the proposed control system, instead of using (41).

Finally, let the blade drag coefficient be $C_{D_0} \in \mathbb{R}$. From [18] and [19], the resultant external moment can be approximated by

$$M_e = \Sigma_{j=1}^4 r_j \times T_j d_j + (-1)^{j+1} Q_j d_j \tag{43}$$

$$Q_j = C_{Q_j} \rho A_p r_p \left(r_p \omega_j\right)^2 \tag{44}$$

where $C_{Q_j} \in \mathbb{R}$ is the torque coefficient [18] given by

$$C_{Q_j} = C_{T_j}\left(\lambda_j + \mu_{z_j}\right) + \frac{C_{D_0} s}{8}\left(1 + 3\mu_{x_j}^2\right). \tag{45}$$

In short, U_e' and M_e' in (2) and (4) are replaced by (36) and (43), respectively, to simulate the quadrotor dynamics under the effects of winds.

B. Position Tracking Control

The parameters of the quadrotor considered in the numerical simulation are as follows:

$$\begin{aligned} m &= 1\,\text{kg}, \quad d_h = 0.2\ \text{m}, \ d_v = 0.01\ \text{m} \\ J &= 10^{-3}\text{diag}[1,1,5]\ \text{kg m}^2, \quad T_{\max} = 8\ \text{N} \\ C_{TQ} &= 0.1\ \text{m}, \ C_\alpha = 1\times 10^{-2}\ \text{rad s m}^{-1} \\ C_d &= 0.01\ \text{kgm}^{-1}, \quad c = 0.01\ \text{m}, \\ N_b &= 2, \quad r_p = 0.1016\ \text{m}. \end{aligned}$$

The controller gains are chosen as

$$\begin{aligned} k_x &= 1, \quad k_v = 1.4, \ k_R = 1.7, \ k_\Omega = 2.4 \\ \gamma_{w_1} &= 1, \quad \gamma_{v_1} = 0.3, \ \kappa_1 = 0.1 \\ \gamma_{w_2} &= 0.3, \quad \gamma_{v_2} = 3, \ \kappa_2 = 0.1, \ N_{2_1} = N_{2_2} = 6. \end{aligned}$$

Initially, the quadrotor is at rest as specified by

$$\begin{aligned} x_0 &= [0,0,0]^{\mathrm{T}}\ \text{m}, \quad v_0 = [0,0,0]^{\mathrm{T}}\ \text{m s}^{-1} \\ R_0 &= I_{3\times 3}, \quad \Omega_0 = [0,0,0]^{\mathrm{T}}\ \text{rad s}^{-1}. \end{aligned}$$

The desired trajectory is a sinusoidal oscillation along the first inertial axis. More specifically

$$x_d(t) = [\cos 2t,\ 0,\ 0]^{\mathrm{T}}\ \text{m} \tag{46}$$

and the desired direction of the first body-fixed axis is

$$b_{1d} = [1,0,0]^{\mathrm{T}}. \tag{47}$$

It is assumed that the wind velocity in the inertial frame is given by

$$v_w = [\sin 2t + \cos 4t, \cos 3t, -0.5]^{\mathrm{T}}\ \text{m s}^{-1}. \tag{48}$$

The corresponding simulation results are presented in Figs. 4 and 5. To illustrate the advantage of the adaptive controller, we also present the simulation results of the geometric controller without using the neural network terms [12]. Specifically, the total thrust and torque are given by (13), (17), and (18) with $\bar{\Delta}_1, \bar{\Delta}_2 = 0_{3\times 1}$. In addition, the simulation result with the geometric PID controller [8] is provided. This controller is designed to compensate for the unknown fixed disturbances to the quadrotor. The results of the three different controllers, the proposed adaptive controller, and the controllers presented in [8] and [12] are denoted by the red dash-dotted line, the blue solid line, and the green dash-dotted line, respectively. The main goal is to track the desired position trajectory given by (46). From Fig. 4, it can be seen that ignoring disturbances in the controller results in failure to track the desired position, especially along the third axis. The geometric PID controller improves the tracking performance over time. However, the proposed controller adapts itself to the disturbances quickly while exhibiting smaller tracking errors. Furthermore, as shown in Fig. 5, although the other two controllers instantly increase the thrust of the first rotor at $t = 0$ to compensate for the initial

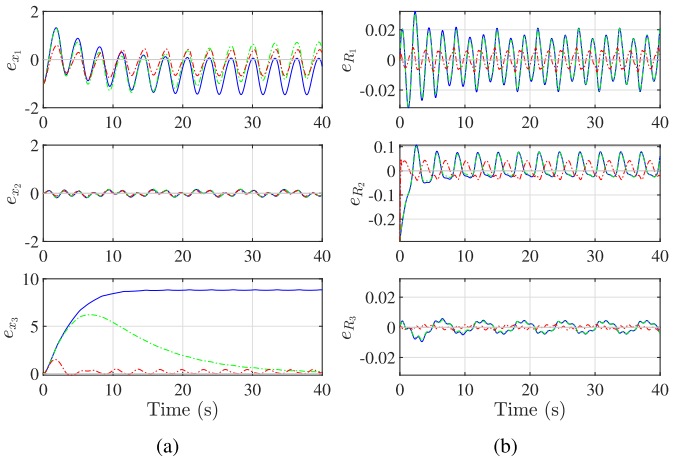

Fig. 4. Position tracking simulation: tracking errors (blue line: without disturbance rejection [12]; green dash-dotted line: PID [8]; and red dash-dotted line: adaptive controller). (a) Position error (m). (b) Attitude error.

error, they fail to adjust the thrust properly afterward, thereby causing large tracking errors, especially along e_{x_3}. However, with the proposed controller, the thrust at each rotor remains in the acceptable range, well under the maximum thrust $T_{\max} = 8$ N. More specifically, the root-mean-square errors along e_{x_3} for the controller without disturbance rejection, PID, and the proposed controller are 8.2, 3.2, and 0.34 m, respectively.

V. Quadrotor UAV Flight Experiments

In this section, the proposed geometric adaptive controller is validated by the flight experiments. Its hardware and software are custom-designed and developed in-house. To demonstrate the capability of rejecting the disturbances, flight experiments are performed under wind disturbances generated by an industrial fan. First, we describe the hardware and software configurations. Then, we present the experimental results in two sections, including attitude and flight trajectory trackings. Additional experimental results are available in [21].

A. Hardware Configuration

The quadrotor platform is shown in Fig. 6. It has four brushless DC electrical motors (700-kV T-Motor) paired with 11 × 3.7 carbon fiber propellers. To control the rotational speed of the motors, each one is connected to an electronic speed control (MikroKopter BL-Ctrl v2), which receives the commands through the Inter-integrated Circuit (I2C) protocols from an onboard computer.

All computations are performed on an embedded system-on-module (NVIDIA Jetson TX2) running a Linux operating system (Ubuntu 16.04 with JetPack 3.3). The onboard computer is attached to an expansion board (Connect Tech's Orbitty Carrier), which is connected to a custom-designed printed circuit board. This board houses a nine-axis inertial measurement unit (IMU; VectorNav VN100) and I2C connection headers for the motor speed controller. The computing module communicates with a ground server (MacBook Pro) through Wi-Fi to receive flight commands and data logging. A single

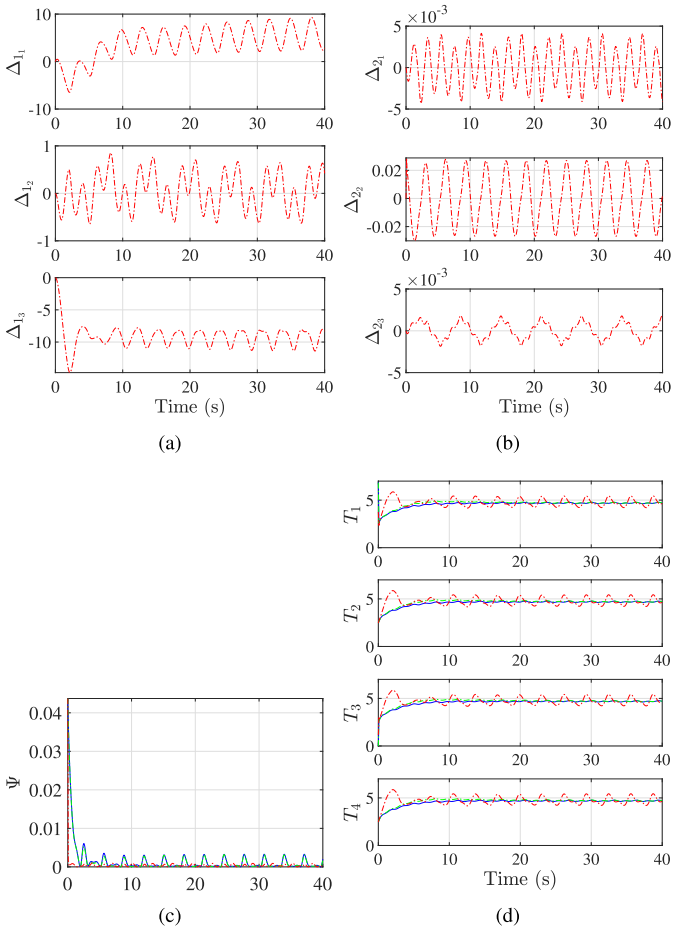

Fig. 5. Position tracking simulation: adaptive terms, attitude tracking error, and thrust (blue line: without disturbance rejection [12]; green dash-dotted line: PID [8]; and red dash-dotted line: adaptive controller). (a) Δ_1 for position. (b) Δ_2 for attitude. (c) Attitude error function. (d) Thrust (N).

Fig. 6. Quadrotor UAV developed in the flight dynamics and control laboratory. (a) Quadrotor UAV. (b) Attitude control test.

14.8-V Li–Po battery provides power for the motors and the onboard computer. An optical motion capture system (VICON) measures the position and orientation of the quadrotor and sends their data through Wi-Fi to the onboard computer, which are fed to an estimator to integrate the measurements from IMU and VICON, and to determine the velocity.

The properties of the quadrotor are given by

$$J = \text{diag}[0.02, 0.02, 0.04]\ \text{kgm}^2, \quad m = 2.1\ \text{kg}, \quad d_h = 0.23\ \text{m}$$

where the inertia matrix is estimated by a CAD model.

To generate wind disturbances in the indoor flight test facility, an industrial pedestal fan (Air King 9175) is placed. The wind speed generated by the fan is measured and presented in Figs. 7 and 10.

B. Flight Software

The flight software is written in C++. We used the POSIX thread library to execute multiple tasks simultaneously. This includes threads for data logging, communication, estimation, and control with the average frequencies of 100, 60, 100, and 400 Hz, respectively. Additional software is developed for the ground server that transmits commands to the quadrotor and receives the flight data from the onboard computer to monitor the quadrotor responses. We used the Glade library to design a graphical user interface. It is used to monitor the flight data and to enhance user interactions. The flight data are saved in the host computer for postprocessing.

C. Attitude Trajectory Tracking Control

We first perform experiments for the attitude control. Here, the quadrotor is attached to a spherical joint to prevent any translation. In particular, the spherical rolling joint (SRJ012C-P from Myostat Motion Control) is affixed to an aluminum bar, as illustrated in Fig. 6(b). It allows up to 30° in roll and pitch, and unlimited yaw.

As the spherical joint is below the mass center, this setup resembles the dynamics of an inverted rigid pendulum, and there is an additional gravitational torque to be considered in (4). As such, the control moment in (18) is augmented by a canceling term. Moreover, the moment of inertia is translated to the center of rotation [21].

The wind speed generated with the fan is measured using a TriSonica-Mini 3-D sonic anemometer as follows. The fan faces the $-e_2$ direction in the inertial frame while generating wind blowing to the left in Fig. 7. The wind generated by the selected fan greatly varies depending on the relative location of the fan, and they are with nontrivial turbulence. To measure these, the quadrotor mounted on a fixed stand is oriented in three different ways within the desired trajectory given by (49). For each configuration, the wind is measured for 15 s with an anemometer placed at the top of a selected rotor. During the measurements, the rotors were not running to avoid disturbing the wind with the rotors' downwash and to solely measure the fan's wind speed. The corresponding results are presented in the inertial frame in Fig. 7, where it is illustrated that the wind speed varies greatly depending on the attitude and the rotor location. As such, each rotor experiences different, time-varying wind, while the quadrotor follows the desired attitude trajectory.

The desired attitude is parameterized as

$$R_d = \begin{bmatrix} c\theta c\phi & s\psi s\theta c\phi - \cos\psi s\phi & c\psi s\theta c\phi + s\psi s\phi \\ c\theta s\phi & s\psi s\theta s\phi + c\psi c\phi & c\psi s\theta s\phi - s\psi c\phi \\ -s\theta & s\psi c\theta & c\psi c\theta \end{bmatrix} \quad (49)$$

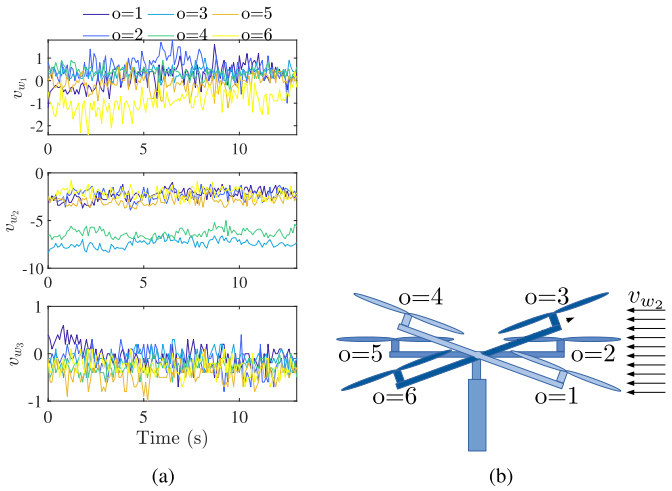

(a) (b)

Fig. 7. Wind measurement for the attitude trajectory tracking test. (a) Wind speed (ms^{-1}) measurement for 15 s at several orientations. (b) Schematic of the quadrotor UAV attitude test.

where cos and sin are shown by c and s, respectively. The Euler angles ψ, θ, and ϕ are chosen as

$$\psi(t) = \pi A_s \cos(2\pi B_s t) \tag{50}$$
$$\theta(t) = \pi A_t \cos(2\pi B_t t) \tag{51}$$
$$\phi(t) = \pi A_f \sin\big(2\pi B_f t\big) \tag{52}$$

and the trajectory parameters are set to

$$A_s = 0.15, \quad A_t = 0.12, \quad A_f = 0.11$$
$$B_s = 0.5, \quad B_t = 0.5, \quad B_f = 0.5. \tag{53}$$

The desired trajectory is chosen such that the vehicle rotates along the three axes of b_1, b_2, and b_3 simultaneously, while wind is blowing toward the direction of $-e_2$ in the inertial frame.

The controller gains and parameters are chosen as

$$k_R = 1.2, \quad k_\Omega = 0.6$$
$$\gamma_{w_2} = 1, \quad \gamma_{v_2} = 0.01, \ \kappa_2 = 0.001, \ c_2 = 1.$$

The number of neurons in the first, hidden, and output layers is

$$N_{1_2} = 6, \quad N_{2_2} = 3, \ N_{3_2} = 3.$$

The number of neurons in the hidden layer has been increased until no further performance is observed. As such, the above neural network structure is sufficiently rich for the uncertainties in the given experiments. The corresponding responses for the three different controllers are presented in Fig. 8. The blue line is for the geometric controller without disturbance rejection [12], the green line is for the geometric controller with an integral term presented in [8], and the red line is for the proposed method.

It can be observed that the geometric controller without disturbance rejection causes large trajectory errors. However, the proposed controller and the controller presented in [8] improve the results [see Fig. 8(d)].

Fig. 9 shows the experimental setup in the $e_2 - e_3$ plane, while the wind is blowing toward $-e_2$, and e_3 points downward. The photograph is taken at the time of 0.5 s when the

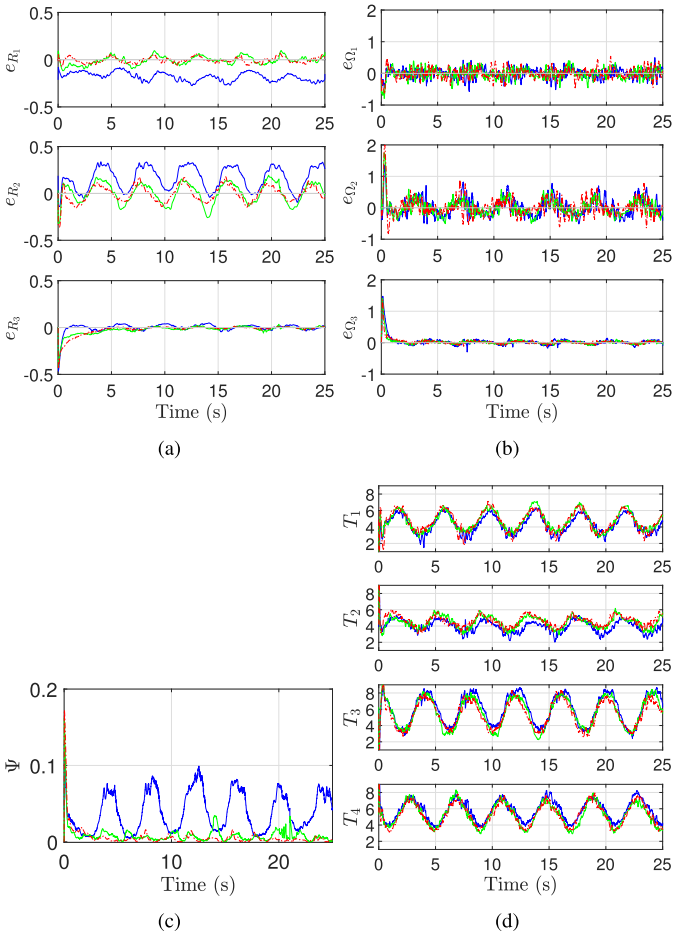

Fig. 8. Attitude tracking experiments: attitude and angular velocity errors, and four rotors' thrusts (blue line: without disturbance rejection [12]; green line: PID [8]; and red dash-dotted line: adaptive controller). (a) Attitude error. (b) Angular velocity error (rad s^{-1}). (c) Attitude error function (Ψ). (d) Thrust (N).

Fig. 9. Attitude tracking experiment: snapshot at $t = 0.5$ s, with the desired pitch angle of $\phi_d = 19.8°$ (left: adaptive controller and right: without disturbance rejection [12]).

desired pitch angle is $\phi_d = 19.8°$. On the left, tracking with the proposed adaptive controller is shown, and on the right, the geometric controller without wind disturbance rejection is presented. It can be seen that there is a large deviation in the desired pitch angle (about $-19.8°$) in the presence of wind in the absence of the disturbance-rejection techniques.[1]

D. Position Trajectory Tracking Control

Next, the quadrotor is detached from the spherical joint used in Section V-C, and it is controlled with the position controller provided in Proposition 1. The quadrotor properties

[1]For the video file of this experiment, visit the FDCL YouTube channel at https://youtu.be/zUsOif1SfEs or the experiment section of the FDCL Website at http://fdcl.seas.gwu.edu/

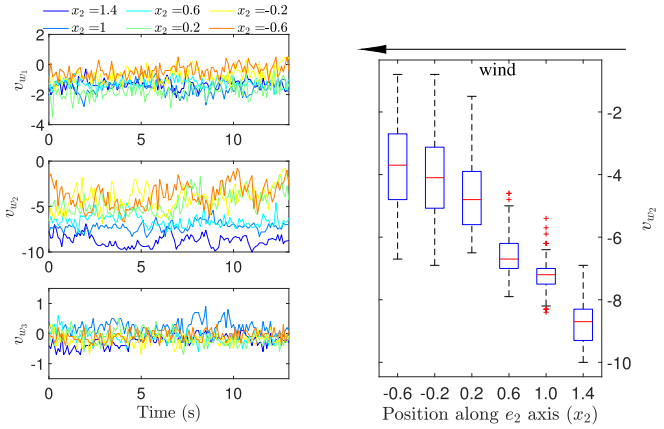

(a) (b)

Fig. 10. Wind measurement for the position trajectory test, where the fan is placed at $x_2 = 1.9$ m along the e_2 axis, and it faces the $-e_2$ direction (toward left). (a) Wind speed (ms^{-1}) measurement for 15 s at several positions. (b) Distribution of wind velocity element v_{w_2} (ms^{-1}) versus position (m) in the front of the fan.

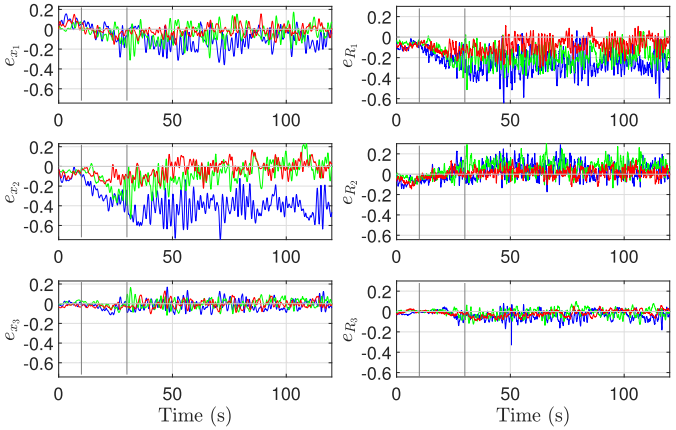

(a) (b)

Fig. 11. Hovering experiments: tracking errors (blue line: without disturbance rejection [12]; green line: PID [8]; and red line: adaptive controller). (a) Position error (m). (b) Attitude error.

are given by

$$J = \mathrm{diag}[0.02, 0.027, 0.04] \ \mathrm{kg\,m}^2, \quad m = 2.1 \ \mathrm{kg}$$
$$d_h = 0.09 \ \mathrm{m}, \quad T_{\max} = 12 \ \mathrm{N}, \quad C_{TQ} = 0.0135 \ \mathrm{m}.$$

To generate the wind disturbances, the fan is placed at $x_2 = 1.9$ m along the second inertial axis e_2, and it faces the $-e_2$ direction in the inertial frame. The wind speed in the front of the fan is measured using a TriSonica-Mini 3-D sonic anemometer. It is held with a long rod at varying distances along the e_2 axis in the front of the fan, and the resulting wind speed measurements are presented in Fig. 10.

1) Geometric Adaptive Control for Hovering: We first study the performance of the proposed adaptive controller for hovering flight when the quadrotor is subject to the wind. Initially, there is no wind. Later, the fan is turned on at about $t = 10$ s and reaches the maximum speed at about $t = 30$ s. The location of the quadrotor along the second inertial axis is 1.0 m and the corresponding average wind speed is about 7.3 m/s, as shown in Fig. 10.

The controller gains and parameters are chosen as

$$k_x = 16.0, \quad k_v = 5.0, \ k_R = 1.2, \ k_\Omega = 0.3$$
$$\gamma_{w_1} = 0.3, \quad \gamma_{v_1} = 0.3, \ \kappa_1 = 0.0001, \ c_1 = 1$$
$$\gamma_{w_2} = 0.035, \quad \gamma_{v_2} = 0.035, \ \kappa_2 = 0.0001, \ c_2 = 1.$$

The number of neurons in the first, hidden, and output layers is

$$N_{1_1} = 6, \quad N_{2_1} = 3, \ N_{3_1} = 3$$
$$N_{1_2} = 6, \quad N_{2_2} = 3, \ N_{3_2} = 3.$$

The experimental results[2] are illustrated in Figs. 11 and 12 with comparisons against a controller without a disturbance-rejection technique [12] and a geometric PID controller [8]. The controller without any disturbance rejection causes a relatively large steady-state error e_{x_2} along the direction of the wind. While the PID controller eliminates such steady errors, it yields a noticeable disruption in position, especially after the fan is turned on, indicated by a vertical line on the figures. Even afterward, the turbulence causes a burst of errors. In contrast, the proposed adaptive controller yields consistent tracking performances throughout the experiment, and compared with the geometric controller without disturbance rejection and PID, it reduces the root-mean-square error in position from 0.42 and 0.17 m, respectively, to 0.10 m, while the total force is reduced from 10.61 and 10.67 N, respectively, to 10.19 N.

2) Geometric Adaptive Control for Position Tracking: Next, the performance of the adaptive controller for trajectory tracking is presented. The desired trajectory is given by

$$x_d(t) = \begin{bmatrix} -0.67 \\ 0.2 - 1.2\cos\left(\frac{\pi t}{12}\right) \\ -1.57 \end{bmatrix}, \quad b_1(t_k) = \begin{bmatrix} 1 \\ 0 \\ 0 \end{bmatrix} \tag{54}$$

which is a sinusoidal oscillation along the second inertial axis. The controller gains and parameters are identical to Section V-D1.

For the presented experiment, the quadrotor operates over various locations in an unsteady nonuniform wind profile generated by the fan, as illustrated in Fig. 10. The desired trajectory is selected such that the relative velocity of the quadrotor to the fan varies. Initially, the quadrotor flies toward the fan. Then, it moves away from the fan, thereby the wind affecting the quadrotor changes from 1 to 10 ms^{-1}, as illustrated in Fig. 10. In short, due to the turbulence from the fan and the maneuvers of the quadrotor, the wind experienced by the quadrotor is not steady for the presented experimental results.

Figs. 13 and 14 show the experimental data. The trajectories without disturbance rejection are plotted in blue line and those with the proposed adaptive controller in red line. It is illustrated that the proposed controller yields smaller tracking errors without excessive rotor thrusts. This illustrates

[2]For the video file of the hover flight experiment, visit the FDCL YouTube channel at https://youtu.be/ouSsrDfi8DM or the experiment section of the FDCL Website at http://fdcl.seas.gwu.edu/

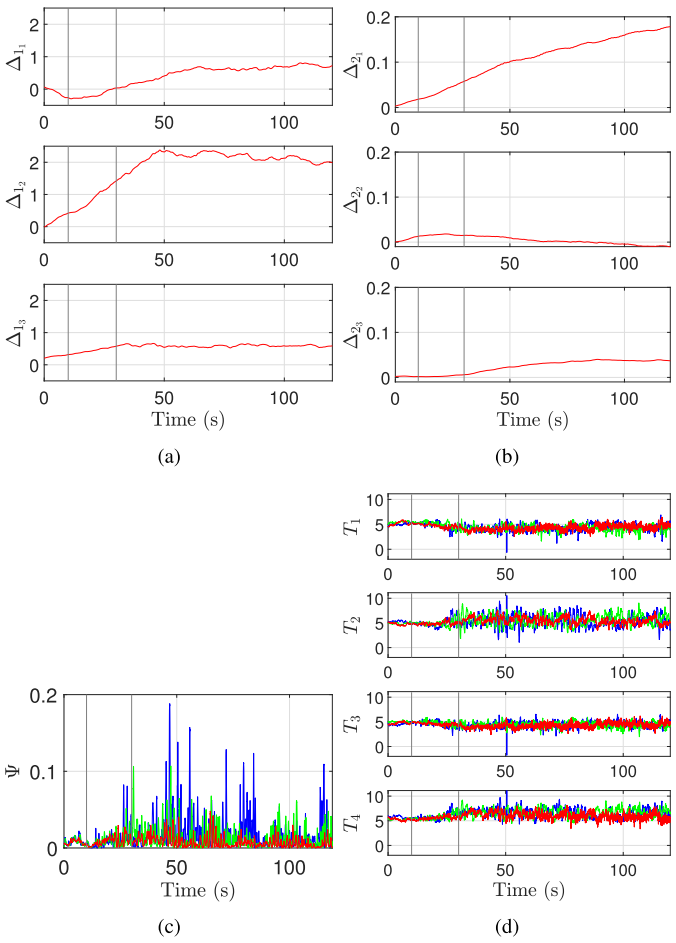

Fig. 12. Hovering experiments: adaptive terms, attitude tracking error, and thrusts (blue line: without disturbance rejection [12]; green line: PID [8]; and red line: adaptive controller). (a) Δ_1 for position. (b) Δ_2 for attitude. (c) Attitude error function. (d) Thrust (N).

that the proposed controller effectively compensates the wind disturbance that may change depending on the position and velocity of the quadrotor relative to the fan, as well as the time-dependent turbulence. More specifically, the adaptive controller decreases the root-mean-square errors of the position tracking from 0.15 to 0.07 m while decreasing the total force from 5.7 to 5.4 N, compared with the controller without disturbance rejection.

3) Geometric Adaptive Control for Backflip: To illustrate the performance of the proposed control system through an agile maneuver, here we present experimental results for a backflip maneuver.

The desired trajectory is composed of the following three sequences: take-off, backflip, and hovering. The quadrotor enters the region of strong wind generated by the fan at the end of the take-off, and it is affected by the unsteady wind throughout the remaining sequences. As such, the unique feature of the proposed adaptive control system that can handle the time-varying, configuration-dependent disturbances is critical to complete this challenging maneuver successfully. First, the quadrotor takes off to reach the desired upward

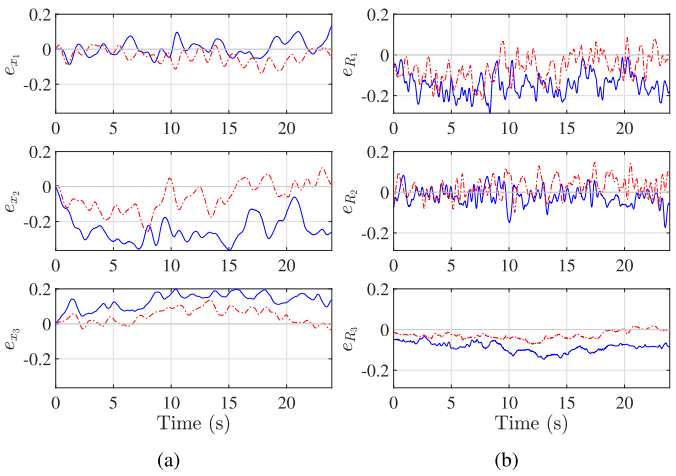

Fig. 13. Position tracking experiments: tracking errors (blue line: without disturbance rejection [12] and red dash-dotted line: adaptive controller). (a) Position error (m). (b) Attitude error.

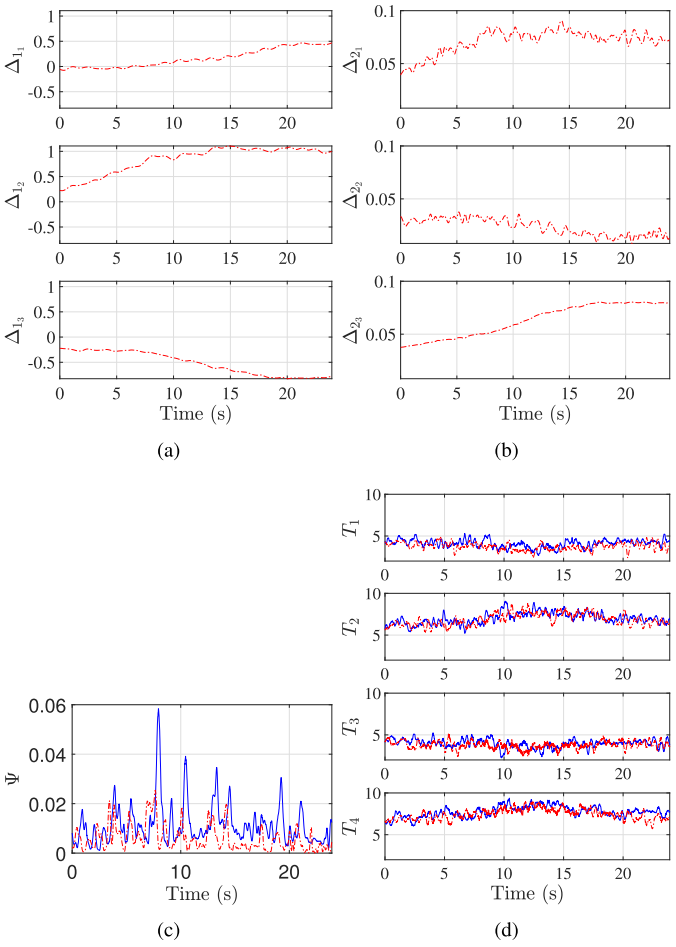

Fig. 14. Position tracking experiments: adaptive terms, attitude tracking error, and thrust (blue line: without disturbance rejection [12] and red dash-dotted line: adaptive controller). (a) Δ_1 for position. (b) Δ_2 for attitude. (c) Attitude error function. (d) Thrust (N).

velocity from $t_0 = 0$ s to $t_1 = 2.20$ s as follows:

$$x_d(t) = x_0 + \frac{at^2}{2}[0, 0, 1]^{\mathrm{T}}, \quad b_{1_d} = [1, 0, 0]^{\mathrm{T}} \tag{55}$$

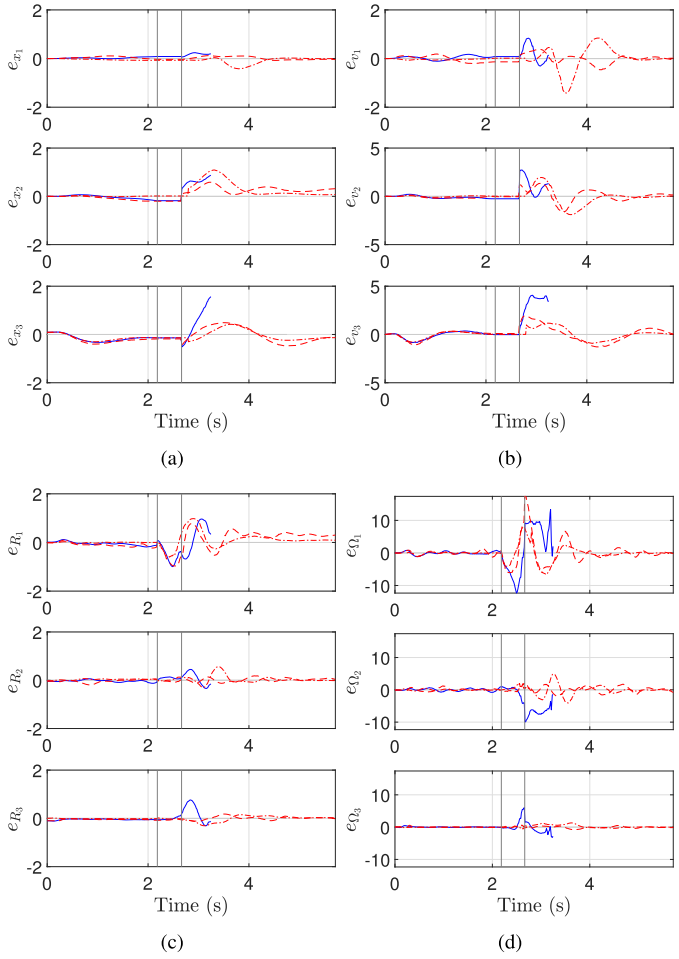

Fig. 15. Backflip experiments: tracking errors (blue line: without disturbance rejection [12] and dash-dotted and dashed red lines: adaptive controller). (a) Position error (m). (b) Velocity error (ms^{-1}). (c) Attitude error. (d) Angular velocity error (rad s^{-1}).

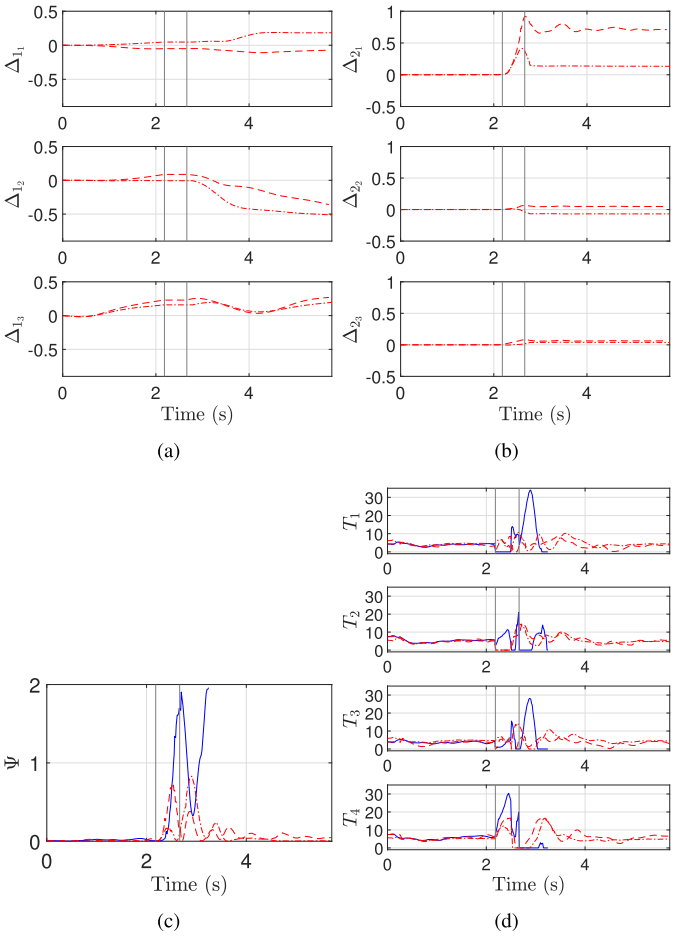

Fig. 16. Backflip experiments: adaptive terms, attitude error function, and thrusts (blue line: without disturbance rejection [12] and dash-dotted and dashed red lines: adaptive controller). (a) Δ_1 for position. (b) Δ_2 for attitude. (c) Attitude error function. (d) Thrust (N).

where $x_0 = [-0.22,\ 0.47,\ -0.50]^{\mathrm{T}}$, $a = -0.50$, and (17) and (18) are used to control the quadrotor.

In the next step, the quadrotor performs a backflip while encountering an unsteady wind shown in Fig. 10. More specifically, the attitude is controlled with (18) to rotate the quadrotor about 360° along the first body-fixed axis b_{1_d}, which is parallel to the first inertial axis e_1 in this configuration. The desired attitude trajectory is chosen as

$$R_d(t) = \exp\left(\theta_d(t)\hat{b}_{1_d}\right) \tag{56}$$

where the rotation angle is chosen as a second-order polynomial function of time

$$\theta_d(t) = \begin{cases} \frac{1}{2}\alpha_m(t-t_1)^2, & \text{if } t_1 < t < t_1 + \frac{\delta t}{2} \\ \frac{1}{2}\Delta_t\alpha_m(t-t_1), & \\ -\frac{1}{2}\alpha_m\left(t - t_1 - \frac{\delta t}{2}\right)^2, & \text{if } t_1 + \frac{\Delta_t}{2} < t < t_1 + \frac{6}{8}\delta t \end{cases} \tag{57}$$

with $\alpha_m = 60.0$ and $\Delta_t = ((8\pi)/\alpha_m)^{1/2}$. The resulting desired angular velocity is

$$\Omega_d(t) = \begin{cases} \alpha_m(t-t_1)b_{1_d}, & \text{if } t_1 < t < t_1 + \frac{\delta t}{2} \\ \alpha_m(\Delta_t + t_1 - t)b_{1_d}, & \text{if } t_1 + \frac{\delta t}{2} < t < t_1 + \frac{6}{8}\delta t. \end{cases} \tag{58}$$

After the backflip, (17) and (18) are used to control the quadrotor to make it hover at a fixed location specified as

$$x_d(t) = x_0 + \frac{at_1^2}{2}[0, 0, 1]^{\mathrm{T}}, \quad b_{1_d} = [1, 0, 0]^{\mathrm{T}}. \tag{59}$$

Figs. 15 and 16 show the experimental results. The trajectories without disturbance rejection are plotted in blue line and with the proposed adaptive controller in red line. The results of the two experiments are presented in a dashed line and a dash-dotted line to illustrate the repeatability. The gray lines are to separate the three stages described earlier. The first gray line divides the take-off from the backflip, and the second one separates the backflip from the last hovering stage. For the control system presented in [12], the angular velocity diverges during the backflip stage, resulting in a large attitude tracking error afterward. More specifically, due to the wind in the $-e_2$ direction, the quadrotor could not complete a swift rotation

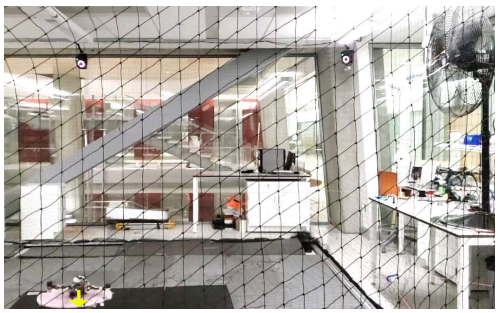

(a)

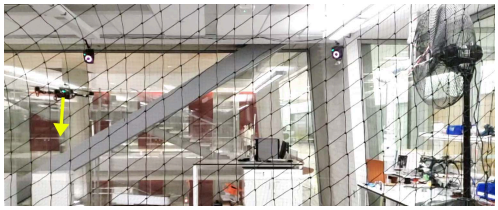

(b)

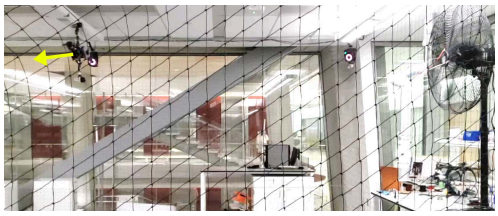

(c)

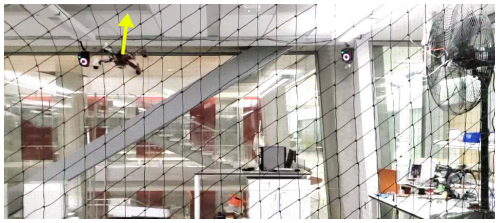

(d)

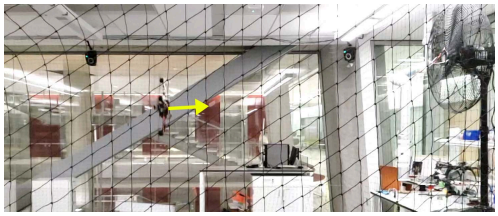

(e)

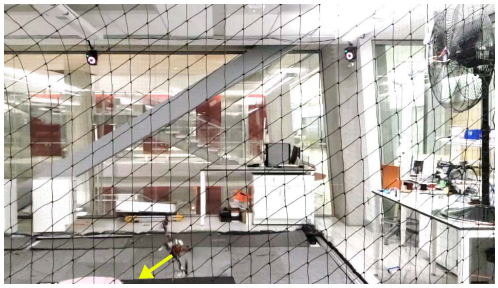

(f)

Fig. 17. Backflip without disturbance rejection [12] (snapshots). (a) At $t = 0$ s. (b) At $t = 2.20$ s. (c) At $t = 2.52$ s. (d) At $t = 2.71$ s. (e) At $t = 2.80$ s. (f) At $t = 3.24$ s.

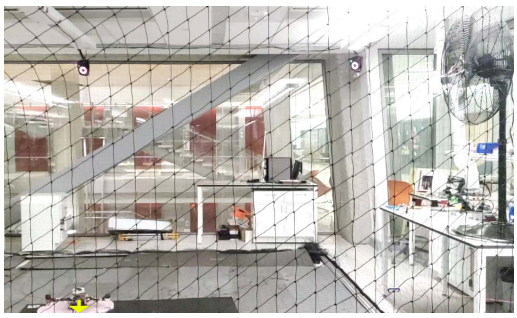

(a)

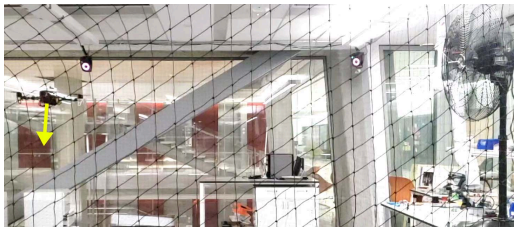

(b)

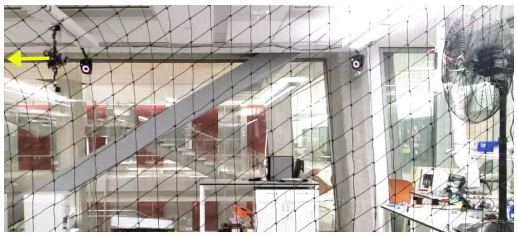

(c)

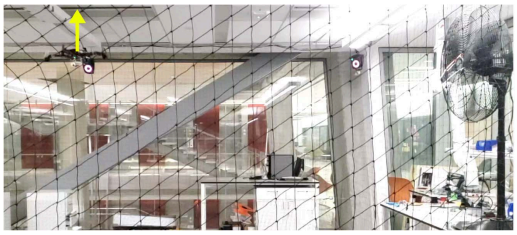

(d)

(e)

(f)

Fig. 18. Backflip with the adaptive controller (snapshots). (a) At $t = 0$ s. (b) At $t = 2.02$ s. (c) At $t = 2.48$ s. (d) At $t = 2.55$ s. (e) At $t = 2.60$ s. (f) At $t = 2.74$ s.

during the second step. It rotated only about 180° along the e_1 axis in the second step and continued the rotation through the third stage, during which the quadrotor fails to regain control and loses height such that the position error along the e_3 axis reaches 1.6 m, as shown in Fig. 15(a). Finally, the quadrotor crashes into the floor at $t = 3.2$ s, where the blue lines end. See Fig. 17 for the snapshots. The yellow arrows indicate the direction of b_3 starting from the center of mass.

In contrast, the proposed geometric adaptive controller with the neural network results in a successful backflip maneuver followed by a stable hovering flight, as illustrated in Fig. 18. The yellow arrows indicate the direction of b_3 starting from the center of mass. Remarkably, the neural network parameters are adjusted promptly over the short period of the second backflip stage to achieve the successful backflip maneuver. Such an agile maneuver under the effects of wind has not been demonstrated before.[3]

VI. Conclusions

We have presented a geometric adaptive control system for a quadrotor UAV based on an artificial neural network. The weight parameters of the neural network are adjusted online such that the effects of the unstructured, arbitrary uncertain forces and moments are mitigated. The efficacy of the proposed approach is illustrated by numerical examples under simulated wind effects and indoor flight experiments under the unsteady spatially varying wind gust generated by an industrial fan. In particular, it is shown that the proposed scheme can successfully and swiftly eliminate the adverse wind effects for an aggressive maneuver. This can be further used in estimating the effects of the wind by the converged values of the weighting parameters.

For a future work, the neural network can be trained offline to generate the expected force and moment for a given wind gust. If the quadrotor UAV is augmented with an on-board anemometer, the proposed adaptive scheme can be used to mitigate the difference between the actual disturbance and the predicted values to improve performance under strong winds.

Appendix

Here, we present the proof of Proposition 1. First, in Section VI-A, selected identities are presented. Then, in Section VI-B, we analyze the error dynamics for a position tracking command, which will be integrated with the attitude error dynamics presented in Section VI-C. Finally, in Section VI-D, we consider the stability of the complete dynamics. An alternative, more involved proof with less conservative results is available in [22].

[3]For the video file of this experiment, visit the FDCL YouTube channel at https://youtu.be/a-DG2PcUu7k or the experiment section of the FDCL Website at http://fdcl.seas.gwu.edu/

A. Identities

For any $\mathcal{A} \in \mathbb{R}^{3\times3}$, $x, y \in \mathbb{R}^3$, $c_1, c_2, c_3 \in \mathbb{R}$

$$\mathrm{tr}\left[yx^{\mathrm{T}}\right] = x^{\mathrm{T}}y \tag{60}$$

$$-c_1x^2 + c_2x \leq -\frac{c_1}{2}x^2 + \frac{c_2^2}{2c_1} \tag{61}$$

$$\mathcal{A}^{\mathrm{T}}\hat{x} + \hat{x}\mathcal{A} = \left(\left[\mathrm{tr}[\mathcal{A}]I_{3\times3} - \mathcal{A}\right]x\right)^{\wedge}. \tag{62}$$

Let $\mathcal{D}$ be an open domain containing the origin of the error states, defined as follows:

$$\begin{aligned}\mathcal{D} = \Big\{ & x, v, R, \Omega, (W_i, V_i)_{i\in\{1,2\}} \in \mathbb{R}^3 \times \mathbb{R}^3 \times \mathsf{SO(3)} \times \mathbb{R}^3 \\ & \times \left(\mathbb{R}^{N_{2_i}+1\times N_{3_i}} \times \mathbb{R}^{N_{1_i}+1\times N_{2_i}}\right)_{i\in\{1,2\}} \| \|e_x\| + \|e_v\| \\ & + \Psi + \|e_\Omega\| + \|\tilde{Z}_1\| + \|\tilde{Z}_2\| < d \Big\}\end{aligned} \tag{63}$$

for a positive constant d. The subsequent Lyapunov analysis is conducted in the domain $\mathcal{D}$.

Here, we show that all the states, namely $(x, v, R, \Omega, \bar{Z}_1, \bar{Z}_2)$, are bounded in $\mathcal{D}$. Recall that from the problem formulation, the desired position trajectory $x_d(t)$ and all its time derivatives are bounded. These imply that $x = e_x + x_d$ and $v = e_v + \dot{x}_d$ are bounded in $\mathcal{D}$. From Assumption (22) and the projection scheme in (24) and (25), the estimated weighting parameters $(\bar{Z}_1, \bar{Z}_2)$ are also bounded.

Throughout this proof, the bound of any state or any error variable within $\mathcal{D}$ is denoted by a single variable δ, i.e., $\|e_x\| \leq \delta$, $\|v\| \leq \delta$. In addition, any function of δ, which is independent of the control parameters, is denoted by δ. This practice is not uncommon in the nonlinear controls [23], and it is to present the key idea of the proposed control system concisely without introducing too many notations.

The second-order derivative of the desired trajectory is sufficiently distinct from the gravitational acceleration, as shown in (10). As such, in (13), the first three terms satisfy

$$\|\bar{\Delta}_1 - k_x e_x - k_v e_v\| \leq (1 + k_x + k_v)\delta$$

and the last two terms satisfy $\|-mge_3 + m\ddot{x}_d\| \geq mB_g$. Thus, when B_g is sufficiently large, the term A that is composed of the sum of the above two cannot vanish, i.e., $A \neq 0$ in $\mathcal{D}$. Therefore, the desired attitude R_c is well defined in (15), and the desired angular velocity Ω_c in (16) and its time derivative are bounded.

Next, we show an inequality that is repeatedly used later in the Lyapunov stability proof. Let $\mathcal{V}_{0_i}$ be the part of the Lyapunov function dependent on $\tilde{W}_i$, $\tilde{V}_i$, which is defined as

$$\mathcal{V}_{0_i} = \frac{1}{2\gamma_{w_i}}\mathrm{tr}\left[\tilde{W}_i^{\mathrm{T}}\tilde{W}_i\right] + \frac{1}{2\gamma_{v_i}}\mathrm{tr}\left[\tilde{V}_i^{\mathrm{T}}\tilde{V}_i\right]. \tag{64}$$

Consider the following expression of $\mathcal{B}_i \in \mathbb{R}$:

$$\mathcal{B}_i = -a_i^{\mathrm{T}}\left(\bar{\Delta}_i\right) + \dot{\mathcal{V}}_{0_i} \tag{65}$$

which will appear in the subsequent stability analysis. Here, we find an upper bound of this term.

The error dynamics of the neural network weights from (29) are given by

$$\dot{\tilde{W}}_i = -\dot{\hat{W}}_i, \quad \dot{\tilde{V}}_i = -\dot{\hat{V}}_i. \tag{66}$$

We substitute (26) and (27) into (66). Using (30), $\mathcal{B}_i$ is rewritten as

$$\begin{aligned}\mathcal{B}_i = a_i^{\mathrm{T}}\Big\{-\tilde{W}_i^{\mathrm{T}}\big[\sigma(z_i)-\sigma'(z_i)z_i\big]-\bar{W}_i^{\mathrm{T}}\sigma'(z_i)\tilde{z}_i+w_i\Big\}\\ +\mathrm{tr}\Big[\tilde{W}_i^{\mathrm{T}}\big[\sigma(z_i)a_i^{\mathrm{T}}-\sigma'(z_i)z_ia_i^{\mathrm{T}}+\kappa_i\bar{W}_i\big]\Big]\\ +\mathrm{tr}\Big[\tilde{V}_i^{\mathrm{T}}\Big\{x_{nn_i}\big[\sigma'(z_i)^{\mathrm{T}}\bar{W}_ia_i\big]^{\mathrm{T}}+\kappa_i\bar{V}_i\Big\}\Big].\end{aligned} \tag{67}$$

Applying (60), it reduces to

$$\mathcal{B}_i = \kappa_i\mathrm{tr}\Big[\tilde{Z}_i^{\mathrm{T}}\bar{Z}_i\Big]+a_i^{\mathrm{T}}(w_i). \tag{68}$$

We have

$$\mathrm{tr}\Big[\tilde{Z}_i^{\mathrm{T}}\bar{Z}_i\Big]=\mathrm{tr}\Big[\tilde{Z}_i^{\mathrm{T}}Z_i\Big]-\mathrm{tr}\Big[\tilde{Z}_i^{\mathrm{T}}\tilde{Z}_i\Big]\le||\tilde{Z}_i||Z_{M_i}-||\tilde{Z}_i||^2. \tag{69}$$

Inequality (61) implies

$$-||\tilde{Z}_i||^2+Z_{M_i}||\tilde{Z}_i||\le-\frac{1}{2}||\tilde{Z}_i||^2+\frac{Z_{M_i}^2}{2}. \tag{70}$$

Since $\|\sigma\|\le 1$, $\|\sigma'\|\le 0.25$, it can be shown that the upper bound for (32) is $\|\mathcal{O}_i\|\le 2+0.25\|\tilde{V}_i\|\|x_{nn_i}\|$. From (22), the upper bound of (31) is

$$\|w_i\|\le 0.25\ V_{M_i}\Big\|\tilde{W}_i\Big\|\Big\|x_{nn_i}\Big\|+W_{M_i}\|\mathcal{O}_i\|+\epsilon_i. \tag{71}$$

Since $\|x_{nn_i}\|\le 1+\|x_{1_i}\|+\|x_{2_i}\|$, $\Big(\Big\|\tilde{W}_i\Big\|,\ \Big\|\tilde{V}_i\Big\|\Big)\le\Big\|\tilde{Z}_i\Big\|$, and (22), we obtain

$$\|w_i\|\le\delta+\delta||\tilde{Z}_i||\Big(1+\Big\|x_{1_i}\Big\|+\Big\|x_{2_i}\Big\|\Big) \tag{72}$$

where $0.25(V_{M_i}+W_{M_i})$ and $2W_{M_i}+\epsilon_i$ are replaced with δ.

Substituting (70) and (71) into (68)

$$\begin{aligned}\mathcal{B}_i\le-\frac{\kappa_i}{2}||\tilde{Z}_i||^2+\frac{\kappa_iZ_{M_i}^2}{2}\\ +\|a_i\|\Big\{\delta+\delta||\tilde{Z}_i||\Big(1+\Big\|x_{1_i}\Big\|+\Big\|x_{2_i}\Big\|\Big)\Big\}.\end{aligned} \tag{73}$$

Since (28), $\|a_1\|\le\|e_v\|+c_1\|e_x\|$, and $\|a_2\|\le\|e_\Omega\|+c_2\|e_R\|$, we have $\|a_i\|\le(1+c_i)\delta$. Since $x_{1_1}=x$ and $x_{2_1}=v$, and $x_{1_2}=E(R)^{\mathrm{T}}$ and $x_{2_2}=\Omega$, we have $\|x_{1_i}\|\le\delta$ and $\|x_{2_i}\|\le\delta$. Again, by invoking our convention on the notation of δ, the above bound can be rewritten as

$$\begin{aligned}\mathcal{B}_i&\le-\frac{\kappa_i}{2}||\tilde{Z}_i||^2+\frac{\kappa_iZ_{M_i}^2}{2}+(1+c_i)\delta\big\{\delta+\delta^3(1+2\delta)\big\}\\ &=-\frac{\kappa_i}{2}||\tilde{Z}_i||^2+(1+c_i)\delta+\frac{\kappa_iZ_{M_i}^2}{2}.\end{aligned} \tag{74}$$

B. Position-Error Dynamics

Taking the derivative of (12) and substituting (2) and (8), the error dynamics are defined as

$$\dot{e}_x = e_v \tag{75}$$

$$m\dot{e}_v = mge_3-\Delta_1-fRe_3-m\ddot{x}_d. \tag{76}$$

Define $\mathcal{X}\in\mathbb{R}^3$ as

$$\mathcal{X}\equiv\frac{f}{e_3^{\mathrm{T}}R_c^{\mathrm{T}}Re_3}\big[\big(e_3^{\mathrm{T}}R_c^{\mathrm{T}}Re_3\big)Re_3-R_ce_3\big] \tag{77}$$

where $e_3^{\mathrm{T}}R_c^{\mathrm{T}}Re_3>0$ [12]. Equation (76) is rewritten as

$$m\dot{e}_v = mge_3-\Delta_1-m\ddot{x}_d-\frac{f}{e_3^{\mathrm{T}}R_c^{\mathrm{T}}Re_3}R_ce_3-\mathcal{X}. \tag{78}$$

Since $b_{3c}=R_ce_3=(-A/\|A\|)$ and $f=-A^{\mathrm{T}}Re_3$, we can conclude that $f=(\|A\|R_ce_3)^{\mathrm{T}}Re_3$. Therefore

$$-\frac{f}{e_3^{\mathrm{T}}R_c^{\mathrm{T}}Re_3}R_ce_3=A. \tag{79}$$

Substituting (13) and (79) into (78), the velocity-error dynamics is written as

$$m\dot{e}_v=-k_xe_x-k_ve_v-\tilde{\Delta}_1-\mathcal{X}. \tag{80}$$

Next, we find the upper bound of $\mathcal{X}$. From (79), $\|A\|=\|-f/(e_3^{\mathrm{T}}R_c^{\mathrm{T}}Re_3)R_ce_3\|$. Since R_ce_3 is a unit vector, $\|A\|=\|-f/(e_3^{\mathrm{T}}R_c^{\mathrm{T}}Re_3)\|$. Consequently, the norm of $\mathcal{X}$ can be written as

$$\|\mathcal{X}\|=\|A\|\Big\|[\big(e_3^{\mathrm{T}}R_c^{\mathrm{T}}\mathrm{Re}_3\big)Re_3-R_ce_3\Big\|. \tag{81}$$

In addition, it is shown that $\|[(e_3^{\mathrm{T}}R_c^{\mathrm{T}}Re_3)Re_3-R_ce_3\|\le\|e_R\|\le\beta<1$, where $\beta=(\psi_1(2-\psi_1))^{1/2}$ [12]. Substituting (13), the upper bound of $\|\mathcal{X}\|$ is given by

$$\|\mathcal{X}\|\le(k_x\|e_x\|+k_v\|e_v\|+\delta)\|e_R\| \tag{82}$$

where it is considered as

$$\Big\|-mge_3+m\ddot{x}_d+\bar{\Delta}_1\Big\|\le\delta. \tag{83}$$

For a nonnegative constant c_1, the Lyapunov function for the position dynamics is chosen as

$$\mathcal{V}_1=\frac{1}{2}k_xe_x^{\mathrm{T}}e_x+\frac{1}{2}me_v^{\mathrm{T}}e_v+mc_1\ e_x^{\mathrm{T}}e_v+\mathcal{V}_{0_1} \tag{84}$$

where $\mathcal{V}_{0_1}$ is given by (64). It is straightforward to show

$$\frac{1}{2}\mathbf{z}_1^{\mathrm{T}}\mathbf{M}_{11}\mathbf{z}_1\le\mathcal{V}_1\le\frac{1}{2}\mathbf{z}_1^{\mathrm{T}}\mathbf{M}_{12}\mathbf{z}_1 \tag{85}$$

where

$$\mathbf{M}_{11}=\begin{bmatrix}k_x & -mc_1 & 0\\ -mc_1 & m & 0\\ 0 & 0 & \dfrac{1}{\min\{\gamma_{w_1},\gamma_{v_1}\}}\end{bmatrix} \tag{86}$$

$$\mathbf{M}_{12}=\begin{bmatrix}k_x & mc_1 & 0\\ mc_1 & m & 0\\ 0 & 0 & \dfrac{1}{\min\{\gamma_{w_1},\gamma_{v_1}\}}\end{bmatrix} \tag{87}$$

$$\mathbf{z}_1=\Big[\|e_x\|,\|e_v\|,\|\tilde{Z}_1\|\Big]^{\mathrm{T}}. \tag{88}$$

If c_1 is sufficiently small such that

$$c_1<\sqrt{\frac{k_x}{m}} \tag{89}$$

then $\mathbf{M}_{11},\mathbf{M}_{12}$ are positive-definite.

Taking the derivative of the Lyapunov function

$$\dot{\mathcal{V}}_1=k_xe_v^{\mathrm{T}}e_x+(e_v+c_1e_x)^{\mathrm{T}}m\dot{e}_v+mc_1e_v^{\mathrm{T}}e_v+\dot{\mathcal{V}}_{0_1} \tag{90}$$

and substituting (80) into (90) and rearranging

$$\begin{aligned}\dot{\mathcal{V}}_1=(mc_1-k_v)e_v^{\mathrm{T}}e_v-c_1\ k_xe_x^{\mathrm{T}}e_x-c_1k_ve_x^{\mathrm{T}}e_v\\ -(e_v+c_1e_x)^{\mathrm{T}}\mathcal{X}-(e_v+c_1e_x)^{\mathrm{T}}\tilde{\Delta}_1+\dot{\mathcal{V}}_{0_1}.\end{aligned} \tag{91}$$

From (82) and $\|e_R\| \leq \beta < 1$, we have

$$\begin{aligned}(e_v + c_1 e_x)^{\mathrm{T}}\mathcal{X} &\leq c_1 k_x \beta \|e_x\|^2 + k_v \beta \|e_v\|^2 \\ &\quad + c_1 k_v \beta \|e_x\|\|e_v\| + c_1 \delta \|e_x\|\|e_R\| + \delta \|e_v\|\|e_R\| \\ &\quad + k_x \|e_x\|\|e_v\|\|e_R\|. \end{aligned} \tag{92}$$

From (28), the last two terms of (91) are the same as (65). Substituting its equivalent expression given by (74) and substituting (92)

$$\begin{aligned}\dot{\mathcal{V}}_1 &\leq -c_1 k_x (1+\beta) e_x^{\mathrm{T}} e_x - (k_v(1+\beta) - m c_1) e_v^{\mathrm{T}} e_v \\ &\quad - \frac{\kappa_1}{2}||\tilde{Z}_1||^2 + c_1 k_v (1+\beta)\|e_x\|\|e_v\| \\ &\quad + c_1 \delta \|e_x\|\|e_R\| + (1+k_x)\delta \|e_v\|\|e_R\| \\ &\quad + (1+c_1)\delta + \frac{\kappa_1 Z_{M_1}^2}{2} \end{aligned} \tag{93}$$

where $\|e_x\| \leq \delta$ is used for the bound of $\|e_x\|\|e_v\|\|e_R\|$.

C. Attitude-Error Dynamics

Here, we analyze the error dynamics for the attitude tracking command.

We calculate the attitude-error dynamics, taking the derivative of (19) and (20) and using (9), (18), and (62). The expression for attitude-error dynamics is given by

$$\dot{e}_R = \frac{1}{2}\big(\mathrm{tr}\big[R^{\mathrm{T}} R_c\big] I_{3\times 3} - R^{\mathrm{T}} R_c\big) e_\Omega \equiv C\big(R_c^{\mathrm{T}} R\big) e_\Omega \tag{94}$$

$$J\dot{e_\Omega} = -k_R e_R - k_\Omega e_\Omega - \tilde{\Delta}_2, \tag{95}$$

$$\dot{\Psi}(R, R_c) = e_R^{\mathrm{T}} e_\Omega \tag{96}$$

$$||C\big(R_c^{\mathrm{T}} R\big)|| \leq 1. \tag{97}$$

For more details about the proof of (94), (96), and (97), see [12].

For a nonnegative constant c_2, the Lyapunov function for the attitude dynamics is defined as

$$\mathcal{V}_2 = \frac{1}{2} e_\Omega^{\mathrm{T}} J e_\Omega + k_R \Psi(R, R_c) + c_2\, e_R^{\mathrm{T}} J e_\Omega + \mathcal{V}_{0_2} \tag{98}$$

where $\mathcal{V}_{0_2}$ is given by (64), and

$$\frac{1}{2}\|e_R\|^2 \leq \Psi(R, R_c) \leq \frac{1}{2-\psi_1}\|e_R\|^2 \tag{99}$$

with $\psi_1 = (1/k_R)[(1/2) e_\Omega(0)^{\mathrm{T}} J e_\Omega(0) + k_R \Psi(R(0), R_c(0))]$. The bounds of $\mathcal{V}_2$ are

$$\frac{1}{2}\mathbf{z}_2^{\mathrm{T}} \mathbf{M}_{21} \mathbf{z}_2 \leq \mathcal{V}_2 \leq \frac{1}{2}\mathbf{z}_2^{\mathrm{T}} \mathbf{M}_{22} \mathbf{z}_2 \tag{100}$$

where

$$\mathbf{M}_{21} = \begin{bmatrix} k_R & -c_2\lambda_{M_J} & 0 \\ -c_2\lambda_{M_J} & \lambda_{m_J} & 0 \\ 0 & 0 & \dfrac{1}{\min\{\gamma_{w_2}, \gamma_{v_2}\}} \end{bmatrix} \tag{101}$$

$$\mathbf{M}_{22} = \begin{bmatrix} \dfrac{2k_R}{2-\psi_1} & c_2\lambda_{M_J} & 0 \\ c_2\lambda_{M_J} & \lambda_{M_J} & 0 \\ 0 & 0 & \dfrac{1}{\min\{\gamma_{w_2}, \gamma_{v_2}\}} \end{bmatrix} \tag{102}$$

$$\mathbf{z}_2 = \Big[\|e_R\|, \|e_\Omega\|, \|\tilde{Z}_2\|\Big]^{\mathrm{T}} \tag{103}$$

with $\lambda_{m_J} = \lambda_m(J)$, $\lambda_{M_J} = \lambda_M(J)$.

Provided that c_2 is sufficiently small to satisfy the following inequality, the matrices $\mathcal{M}_{21}$ and $\mathcal{M}_{22}$ are positive-definite:

$$c_2 < \min\left\{\frac{\sqrt{k_R \lambda_{m_J}}}{\lambda_{M_J}}, \quad \sqrt{\frac{2k_R}{\lambda_{M_J}(2-\psi_1)}}\right\} \tag{104}$$

where $\psi_1 < 2$.

The time derivative of the Lyapunov function is given by

$$\dot{\mathcal{V}}_2 = (e_\Omega + c_2 e_R)^{\mathrm{T}} J \dot{e}_\Omega + k_R \dot{\Psi}(R, R_c) + c_2 \dot{e}_R^{\mathrm{T}} J e_\Omega + \dot{\mathcal{V}}_{0_2}. \tag{105}$$

Substituting the error dynamics (4), (18), and (94)–(97)

$$\begin{aligned}\dot{\mathcal{V}}_2 = (e_\Omega + c_2 e_R)^{\mathrm{T}}\Big(-k_R e_R - k_\Omega e_\Omega - \tilde{\Delta}_2\Big) \\ + k_R e_R^{\mathrm{T}} e_\Omega + c_2\, C\big(R_c^{\mathrm{T}} R\big) e_\Omega^{\mathrm{T}} J e_\Omega + \dot{\mathcal{V}}_{0_2}. \end{aligned} \tag{106}$$

From (97) and $\|J\| \leq \lambda_{M_J}$

$$\begin{aligned}\dot{\mathcal{V}}_2 \leq -c_2 k_R e_R^{\mathrm{T}} e_R + c_2\, k_\Omega ||e_R||||e_\Omega|| - \big(k_\Omega - c_2\lambda_{M_J}\big) e_\Omega^{\mathrm{T}} e_\Omega \\ - (e_\Omega + c_2 e_R)^{\mathrm{T}}\Big(\tilde{\Delta}_2\Big) + \dot{\mathcal{V}}_{0_2}. \end{aligned} \tag{107}$$

From (28), the last two terms of this expression are identical to (65). Substituting its equivalent expression given by (74), we have

$$\begin{aligned}\dot{\mathcal{V}}_2 \leq -c_2 k_R e_R^{\mathrm{T}} e_R + c_2 k_\Omega ||e_R||||e_\Omega|| - \big(k_\Omega - c_2\lambda_{M_J}\big) e_\Omega^{\mathrm{T}} e_\Omega \\ - \frac{\kappa_2}{2}||\tilde{Z}_2||^2 + (1+c_2)\delta + \frac{\kappa_2 Z_{M_2}^2}{2}. \end{aligned} \tag{108}$$

D. Stability Proof for Quadrotor Dynamics

Here, we combine the position-error dynamics and the attitude-error dynamics to show the stability properties of the complete controlled quadrotor. The Lyapunov function is chosen as $\mathcal{V} = \mathcal{V}_1 + \mathcal{V}_2$, where $\mathcal{V}_1, \mathcal{V}_2$ are given by (84) and (98). From (85) and (100), the bound on $\mathcal{V}$ is given by

$$\begin{aligned}\frac{1}{2}\lambda_m(\mathbf{M}_{11})||\mathbf{z}_1||^2 + \frac{1}{2}\lambda_m(\mathbf{M}_{21})||\mathbf{z}_2||^2 \leq \mathcal{V} \leq \frac{1}{2}\lambda_M(\mathbf{M}_{12})||\mathbf{z}_1||^2 \\ + \frac{1}{2}\lambda_M(\mathbf{M}_{22})||\mathbf{z}_2||^2. \end{aligned} \tag{109}$$

It can be rewritten in the form of

$$\frac{1}{2}\mathbf{z}^{\mathrm{T}}\mathbf{M}_1\mathbf{z} \leq \mathcal{V} \leq \frac{1}{2}\mathbf{z}^{\mathrm{T}}\mathbf{M}_2\mathbf{z} \tag{110}$$

where $\mathbf{M}_1, \mathbf{M}_2 \in \mathbb{R}^{2\times 2}$ and $\mathbf{z} \in \mathbb{R}^2$ are

$$\mathbf{M}_1 = \begin{bmatrix} \lambda_m(\mathbf{M}_{11}) & 0 \\ 0 & \lambda_m(\mathbf{M}_{21}) \end{bmatrix}$$

$$\mathbf{M}_2 = \begin{bmatrix} \lambda_M(\mathbf{M}_{12}) & 0 \\ 0 & \lambda_M(\mathbf{M}_{22}) \end{bmatrix}$$

$$\mathbf{z} = [\|\mathbf{z_1}\|, \|\mathbf{z_2}\|]^{\mathrm{T}}.$$

The matrices $\mathbf{M}_1$ and $\mathbf{M}_2$ are positive-definite if (89) and (104) are satisfied.

The derivative of the Lyapunov function is $\dot{\mathcal{V}} = \dot{\mathcal{V}}_1 + \dot{\mathcal{V}}_2$. From (93) and (108), it can be written as

$$\begin{aligned}\dot{\mathcal{V}} &\leq -\mathbf{z}_1^{\mathrm{T}}\mathbf{W}_1\mathbf{z}_1 + \mathbf{z}_1^{\mathrm{T}}\mathbf{W}_{12}\mathbf{z}_2 - \mathbf{z}_2^{\mathrm{T}}\mathbf{W}_2\mathbf{z}_2 + C \\ &\leq -\mathbf{z}^{\mathrm{T}}\mathbf{W}\mathbf{z} + C \end{aligned} \tag{111}$$

where $C = (2 + c_1 + c_2)\delta + (\kappa_1 Z_{M_1}^2)/2 + (\kappa_2\ Z_{M_2}^2)/2$ and

$$\mathbf{W}_1 = \begin{bmatrix} c_1\ k_x(1+\beta) & -\frac{1}{2}c_1\ k_v(1+\beta) & 0 \\ -\frac{1}{2}c_1\ k_v(1+\beta) & k_v(1+\beta) - mc_1 & 0 \\ 0 & 0 & \frac{\kappa_1}{2} \end{bmatrix}$$

$$\mathbf{W}_{12} = \begin{bmatrix} c_1\delta & 0 & 0 \\ (1+k_x)\delta & 0 & 0 \\ 0 & 0 & 0 \end{bmatrix}, \quad \mathbf{W} = \begin{bmatrix} \lambda_m(\mathbf{W_1}) & \frac{1}{2}\|\mathbf{W_{12}}\|_2 \\ \frac{1}{2}\|\mathbf{W_{12}}\|_2 & \lambda_m(\mathbf{W_2}) \end{bmatrix}$$

$$\mathbf{W}_2 = \begin{bmatrix} c_2\ k_R & -\frac{1}{2}c_2\ k_\Omega & 0 \\ -\frac{1}{2}c_2\ k_\Omega & k_\Omega - c_2\lambda_{M_J} & 0 \\ 0 & 0 & \frac{\kappa_2}{2} \end{bmatrix}.$$

If the constants c_1, c_2 are chosen sufficiently small such that

$$c_1 < \min\left\{\sqrt{\frac{k_x}{m}}, \frac{4\ k_v k_x + 4\beta k_v k_x}{4\ k_x m + \beta k_v^2 + k_v^2}, \frac{k_v(1+\beta)}{m}\right\}$$

$$c_2 < \min\left\{\frac{\sqrt{k_R\lambda_{m_J}}}{\lambda_{M_J}}, \sqrt{\frac{2k_R}{\lambda_{M_J}(2-\psi_1)}}, \frac{4\ k_R k_\Omega}{k_\Omega^2 + 4\lambda_{M_J} k_R}, \frac{k_\Omega}{\lambda_{M_J}}\right\}$$

then all the matrices, namely, $\mathbf{M}_{i1}$, $\mathbf{M}_{i2}$, $\mathbf{M}_i$, and $\mathbf{W}_i$ for $i \in \{1, 2\}$ become positive-definite. Furthermore, if k_R, k_Ω are sufficiently large such that

$$\lambda_m(\mathbf{W}_2) > \frac{\|\mathbf{W}_{12}\|^2}{4\lambda_m(\mathbf{W}_1)}$$

then $\mathbf{W}$ becomes positive-definite. Consequently, we have $\dot{\mathcal{V}} \leq -\lambda_m(\mathbf{W})\|\mathbf{z}\|^2 + C$, and for $0 < \theta < 1$

$$\dot{\mathcal{V}} \leq -(1-\theta)\lambda_m(\mathbf{W})\|\mathbf{z}\|^2 \quad \text{if } \|\mathbf{z}\| \geq \sqrt{\frac{C}{\theta\lambda_m(\mathbf{W})}}.$$

Therefore, according to [23, Corollary 5.3], all the error states are uniformly ultimately bounded.

ACKNOWLEDGMENT

The authors would like to thank K. Gamagedara for his valuable contribution to the development of the quadrotor hardware platform used for the experimental validation in this article and also for his kind support.

REFERENCES

[1] R. Gill and R. D'Andrea, "Propeller thrust and drag in forward flight," in *Proc. IEEE Conf. Control Technol. Appl. (CCTA)*, Aug. 2017, pp. 73–79.
[2] W. Craig, D. Yeo, and D. A. Paley, "Dynamics of a rotor-pendulum with a small, stiff propeller in wind," in *Proc. ASME Dyn. Syst. Control Conf. (DSCC)*, vol. 1, no. DSCC2016-9774. New York, NY, USA: ASME, Oct. 2016, Art. no. V001T05A001.
[3] M. Bisheban and T. Lee, "Computational geometric system identification for the attitude dynamics on SO(3)," *Int. J. Control, Autom. Syst.*, vol. 15, no. 6, pp. 2776–2785, Dec. 2017, doi: 10.1007/s12555-016-0714-2.
[4] M. Bisheban and T. Lee, "Computational geometric identification for quadrotor dynamics in wind fields," in *Proc. IEEE Conf. Control Technol. Appl. (CCTA)*, Kohala Coast, HI, USA, Aug. 2017, pp. 1153–1158.
[5] N. K. Tran, E. Bulka, and M. Nahon, "Quadrotor control in a wind field," in *Proc. Int. Conf. Unmanned Aircr. Syst. (ICUAS)*, Jun. 2015, pp. 320–328.
[6] M. Bangura and R. Mahony, "Thrust control for multirotor aerial vehicles," *IEEE Trans. Robot.*, vol. 33, no. 99, pp. 1–16, Apr. 2017.
[7] W. S. Craig, D. W. Yeo, and D. A. Paley, "Geometric control of a quadrotor in wind with flow sensing and thrust constraints: Attitude and position control," in *Proc. AIAA Scitech Forum*, Jan. 2019, p. 1192.
[8] F. Goodarzi, D. Lee, and T. Lee, "Geometric nonlinear PID control of a quadrotor UAV on SE(3)," in *Proc. Eur. Control Conf. (ECC)*, Jul. 2013, pp. 3845–3850.
[9] F. A. Goodarzi, D. Lee, and T. Lee, "Geometric adaptive tracking control of a quadrotor unmanned aerial vehicle on SE(3) for agile maneuvers," *J. Dyn. Syst., Meas., Control*, vol. 137, no. 9, pp. 1–13, Sep. 2015.
[10] D. Mellinger, N. Michael, and V. Kumar, "Trajectory generation and control for precise aggressive maneuvers with quadrotors," *Int. J. Robot. Res.*, vol. 31, no. 5, pp. 664–674, Apr. 2012.
[11] C. Nicol, C. J. B. Macnab, and A. Ramirez-Serrano, "Robust neural network control of a quadrotor helicopter," in *Proc. Can. Conf. Electr. Comput. Eng.*, May 2008, pp. 001233–001238.
[12] T. Lee, M. Leok, and N. McClamroch, "Geometric tracking control of a quadrotor UAV on SE(3)," in *Proc. IEEE Conf. Decis. Control*, Atlanta, GA, USA, Dec. 2010, pp. 5420–5425.
[13] M. Bisheban and T. Lee, "Geometric adaptive control for a quadrotor UAV with wind disturbance rejection," in *Proc. IEEE Conf. Decis. Control (CDC)*, Dec. 2018, pp. 2816–2821.
[14] K. Hornik, M. Stinchcombe, and H. White, "Multilayer feedforward networks are universal approximators," *Neural Netw.*, vol. 2, no. 5, pp. 359–366, Jan. 1989.
[15] P. A. Ioannou and J. Sun, *Robust Adaptive Control*. Upper Saddle River, NJ, USA: Prentice-Hall, 1995.
[16] T. Lee and Y. Kim, "Nonlinear adaptive flight control using backstepping and neural networks controller," *J. Guid., Control, Dyn.*, vol. 24, no. 4, pp. 675–682, Jul. 2001.
[17] T. Lee, M. Leok, and N. McClamroch, "Nonlinear robust tracking control of a quadrotor UAV on SE(3)," *Asian J. Control*, vol. 15, no. 2, pp. 391–408, Mar. 2013.
[18] G. D. Padfield, *Helicopter Flight Dynamics: The Theory and Application of Flying Qualities and Simulation Modelling*. Hoboken, NJ, USA: Wiley, 2007.
[19] G. M. Hoffmann, H. Huang, S. L. Waslander, and C. J. Tomlin, "Precision flight control for a multi-vehicle quadrotor helicopter testbed," *Control Eng. Pract.*, vol. 19, no. 9, pp. 1023–1036, Sep. 2011.
[20] N. Sydney, B. Smyth, and D. A. Paley, "Dynamic control of autonomous quadrotor flight in an estimated wind field," in *Proc. 52nd IEEE Conf. Decis. Control*, Dec. 2013, pp. 3609–3616.
[21] M. Bisheban, "Geometric estimation and control of quadrotor UAVs in wind fields," Ph.D. dissertation, Mech. Aerosp. Eng. Dept., George Washington Univ., Washington, DC, USA, 2018.
[22] M. Bisheban and T. Lee, "Geometric adaptive control for a quadrotor UAV with wind disturbance rejection," 2018, *arXiv:1803.06363*. [Online]. Available: http://arxiv.org/abs/1803.06363
[23] H. Khalil, *Nonlinear Systems*. Upper Saddle River, NJ, USA: Prentice-Hall, 1996.

Mahdis Bisheban received the Ph.D. degree in mechanical and aerospace engineering at the George Washington University, Washington, DC, USA, in 2018.

Her interest includes the control and application of artificial intelligence on autonomous vehicles.

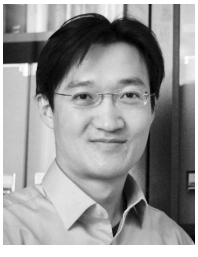

Taeyoung Lee (Member, IEEE) received the Ph.D. degree in aerospace engineering and the master's degree in mathematics from the University of Michigan, Ann Arbor, MI, USA, in 2008.

He is currently a Professor with the Department of Mechanical and Aerospace Engineering, George Washington University, Washington, DC, USA. His research interest includes geometric mechanics and control with applications to complex aerospace systems.